Journal of Applied Physics

RESEARCH ARTICLE | MAY 04 2023

Mimicking bacterial learning and memory in tungsten based two-sided single layers of WSeO, WSeS, WSeSe, and WSeTe

Aykut Turfanda ✉ ; Hilmi Ünlü

Journal of Applied Physics 133, 174301 (2023)
https://doi.org/10.1063/5.0139576

AIP Publishing

Journal of Applied Physics ARTICLE scitation.org/journal/jap

Mimicking bacterial learning and memory in tungsten based two-sided single layers of WSeO, WSeS, WSeSe, and WSeTe

Cite as: J. Appl. Phys. **133**, 174301 (2023); doi: 10.1063/5.0139576
Submitted: 21 December 2022 · Accepted: 17 April 2023 ·
Published Online: 4 May 2023

Aykut Turfanda[1,a)] and Hilmi Ünlü[1,2,b)]

AFFILIATIONS

[1]Nanoscience and Nanoengineering Programme, Istanbul Technical University, Maslak, Istanbul 34467, Türkiye
[2]Department of Electrical and Electronics Engineering, Faculty of Engineering, Fatih Sultan Mehmet Vakif University, Beyoğlu, Istanbul 34445, Türkiye

[a)]**Author to whom correspondence should be addressed:** turfandaa@itu.edu.tr
[b)]**Electronic mail:** hunlu@itu.edu.tr

ABSTRACT

We mimic bacterial learning and memory abilities in tungsten based two-sided single layers of WSeO, WSeS, WSeSe, and WSeTe, where the thickness of the material represents the growth in time. We aim to create a quantum memristor like system to show learning and memory abilities of bacteria with time while it grows. Its governing equation is derived, and it was found to be similar to the gene regulatory response model of the bacteria. Polarization is calculated from the Berry phase theory to plot its relation with the *degauss* parameter in time, which leads to bow-tie like memory switches similar to phase-change memories. We attribute this behavior to a specific bacteria, that is, *Geobacter metallireducens*. Mimicking bacteria's learning and memory abilities will open a way to merge physical intelligence with quantum computing computationally.

I. INTRODUCTION

The current literature in neuromorphic materials and devices is based on showing how well one can mimic the characteristics of neural and synaptic dynamics of the human brains in terms of measurable quantities in materials science and memory device physics, such as current, voltage, conductance, and so on. This aim is to replace the von Neumann computers with the neuromorphic ones by mimicking Human's neural dynamics. This effort is usually realized in memristive or resistive switching devices. Even though there are commercially available products that are believed to realize neuromorphic computing, von Neumann computers in the market cannot be replaced because von Neumann computers have high storage capabilities and have high computational speeds in general compared to the current state of the art of neuromorphic materials.[1] Therefore, we propose to use bacteria's learning and memory dynamics to replace the von Neumann computers instead of emulating the human brain.

Bacteria surround the earth from deep layers of its crust to the human body. They are regarded as one of the earliest forms of life with superb ability of adaptation; they can survive under extreme conditions of temperature and pressure.[2] Bacteria have not only superpowers like living at extremely hot, cold, pressurized, or radiative environments, but also some species are living together with humans. This relationship might be beneficial for both parts; on the other hand, a pathogenic bacteria can be related to some diseases in the human. Even if the usage of bacteria in the drug delivery inside the human body, in cancer curing, and in manipulation of genes in the human by mimicking their defense mechanisms are shown, their abilities of learning and memory are not emulated using two-dimensional materials in the literature to the best of our knowledge.[3–5]

Humans or eukaryotes learning and memory abilities are mimicked by realizing their synapses's characteristic features, such as depression, potentiation, and so on. In the literature, it is

customary to denote pre- and post- synaptic terminals of these kinds of artificial synapses; for example, Tian *et al.* reported an artificial synapse with tunable plasticity based on a twisted bilayer graphene, where a field-effect geometry based resistive memory is proposed, and pre- and post- synaptic terminals are stated.[6] In this way, the main element responsible for the prokaryote's and mainly the bacteria's learning and memory abilities might be defined as the postsynaptic terminal only as depicted by various researchers in analogy to realization of human synapses with two-dimensional materials, even though there are no synapses in the bacteria.[7–9] Bacteria's learning and memory abilities are modeled as a sensory membrane, which is surrounding the bacteria's cell. Many bacteria are small in size and has large surface areas. We show how its surface area described by its membrane and its genetic material is significant for learning and memory. Genetic material dominates the bacterial organisms.

We try to realize a bacteriomorphic material by establishing a quantum memristor like and measurement-induced phase-transition like systems, where the quantum information dynamics are important. However, this is just an analogy because at the macroscopic level, our system is neither a spin qubit nor a single photon. We picked tungsten based two-sided single layers of WSeO, WSeS, WSeSe, and WSeTe to realize this membrane and its growth in time from WSeO to WSeTe. We observe bow-tie-like memory switches in its current–voltage like relation derived from its polarization vs magnitude of smearing, *degauss*, plots, which are very similar to the phase-change like memories. We develop a model mainly based on electrostatic interactions between the bacterial membrane and the metal for bacterial learning and memory by inspiring from the bacteria called *Geobacter metallireducens*.

The model that we developed is tested through the density functional theory, DFT, simulations by tuning *degauss* and showing its relation with the Berry phase theory of polarization. Then, we develop a differential equation to depict the characteristics of the proposed model. After that, we generalize this model by matching its terms with the gene regulatory response of the bacteria. Finally, we modify a learning experiment done for a single-celled organism in the literature for our case to show how well the learning can be depicted with our model through DFT simulations. We report how and why we mimic the bacterial learning and memory abilities, and we discuss the relationship between bacterial growth, genes, adaptation, memory, and learning abilities using the methods of DFT.

II. COMPUTATIONAL METHODS

Quantum ESPRESSO based DFT is performed with optimized norm-conserving Vanderbilt pseudopotentials, 100 Ry kinetic energy cutoff, and a $12 \times 12 \times 2$ Monkhorst–Pack grid.[10–15] A crystallographic information file of bulk WSeSe is retrieved from the Materials Project website.[16] First, bulk WSeSe is optimized with the variable-cell relaxation, where the total energy convergence criterion is set to 10^{-8} Ry and force convergence criterion is set to 10^{-6} Ry/Bohr, with dispersion correction DFT-D3.[17] We obtain a single layer of WSeSe. Then, WSeO, WSeTe, and WSeS single layers are obtained by replacing Se in WSeSe with O, Te, or S. After that, variable-cell relaxation calculation of Quantum ESPRESSO is done in x and y unit cell vector directions, where we ensure at least 20 Å of spacing between the periodic images of a single layer. Their lattice vectors and atomic positions are optimized with a total energy convergence criterion of 10^{-7} Ry and a force convergence criterion of 10^{-5} Ry/Bohr. In electronic structure calculations, a 0.01 Ry *degauss* value with Marzari–Vanderbilt smearing is used to locate the Fermi energy level and the PBE functional is used.[18]

Total polarization is studied using the Berry phase theory of polarization calculations by assuming the system as an insulator. However, to study the effect of a *degauss* parameter in polarization calculations, Fermi–Dirac smearing is used for self-consistent field calculations with varying *degauss* values, and fixed occupations are used for the non-self-consistent field (NSCF) calculations. The magnitude of the absolute polarization density in the z-direction is referred as polarization in the text, which is found from the calculations carried out using the *lberry* keyword of the Quantum ESPRESSO. In these calculations, the number of k-point strings in the third lattice vector's direction, *nppstr*, and k-mesh in the z-direction is taken as 10, where we used converged cut-off energy and a k-grid with respect to the total DFT energy, where the convergence criterion is at least 10^{-3} Ry per atom.

Macroscopic dielectric constants are calculated using density functional perturbation theory as it is implemented in the *ph.x* executable, and its value in the z-direction is read from the diagonal of the macroscopic dielectric constant's matrix. Phonon dispersion calculations based on density functional perturbation theory are performed using a $3 \times 3 \times 1$ grid of q-points with PAW pseudo potentials.[19] Real-time linear response calculations are done by perturbing the system with a positive valued delta function electric field in the YAMBO code, where the output spectrum, the Berry phase polarization in the z-direction vs time, is recorded by considering nine bands above the Fermi energy level and nine bands below the Fermi energy level.[20,21] Crystal orbital Hamilton population, COHP, analysis is done using the LOBSTER code, where the PAW type pseudopotentials are used, and the basis functions for Se are taken as 3d, 4p, and 4s; for W are taken as 5d, 5p, 5s, and 6s; for S are taken as 3p and 3s; for O are taken as 2p and 2s; and for Te are taken as 5p and 5s.[22–24] Bader analysis based on charge density files is performed using a Bader program from Henkelman's group.[25]

Susceptibility tensor's zz element is calculated using time-dependent density functional theory, TDDFT, with 2000 Lanczos iterations and with extrapolation of Lanczos coefficients in the Environ module, where the self-consistent field calculations are done at the gamma point, in different environments, these are, chloroform, where the static permittivity is set to 4.81 and optical permittivity is set to 1.15; ethanol, where the static permittivity is set to 24.5 and optical permittivity is set to 1.69; water, where the static permittivity is set to 80.1 and optical permittivity is set to 1.82; acetone, where the static permittivity is set to 20.7 and optical permittivity is set to 2.85; dimethyl sulfoxide, where the static permittivity is set to 46.7 and optical permittivity is set to 3.9; and nitrobenzene, where the static permittivity is set to 34.82 and optical permittivity is set to 4.02.[26,27]

Wannier interpolated bands are found using the Wannier90 code, where we consider the results obtained from the projected density of states calculations to set the projections to generate the Wannier interpolated bands; these are W's d, Se's s, and p, and O's s and p orbitals for WSeO; W's d, Se's s and p, and S's s and p orbitals for WSeS; W's d, Se's s and p, and Se's s and p orbitals for WSeSe; and W's s and d, Se's s and p, and Te's s and p orbitals for

WSeTe.[28] Ordinary magnetoresistance calculations are done using WannierTools considering the ninth occupied Kohn–Sham, KS, the DFT band and setting the Fermi energy level to 0.026 eV above the valence band maximum.[29] Voigt–Reuss–Hill averaged, from Voigt and Reuss approximations, the Poisson ratio, Young's modulus, and the variation of entropy with temperature are found using a thermo_pw module.[30] Visualization and creation of structures are done using VESTA.[31] ABINIT is used to perform polarization calculations in the Berry phase theory with a finite electric field, which ranges from 0 to around 0.0002 au in the z-direction (1 au of electric field is equal to 514 220 624 373.482 V/m). We used Quantum ESPRESSO optimized geometries, pseudopotentials, k-points, and kinetic energy cutoff during the ABINIT run.[32,68]

III. RESULTS AND DISCUSSION

A. Tungsten based two-sided single layers as a bacterial membrane in time

We model the bacterial learning and memory abilities by inspiring from behaviors of bacteria in the nature, where the researchers showed that bacteria can tailor its membrane by adding amino acids to the polar head group of the phospholipids located in its membrane, and by doing this, bacteria can adapt itself to new conditions that they will be faced.[33] This will constitute the base of our model. In this way, we picked WSeO, WSeS, WSeSe, and WSeTe single layers, which are assumed to be the infinitesimal segment of the bacteria's membrane in time as shown in Figs. 1(a) and 1(b). The change in the thickness of single layers is assumed to be the strain applied in the z-direction because thicknesses are increasing from WSeO to WSeTe. While it grows, the uppermost atom in these single layers is changing, which is assumed to represent the growth of the bacteria, where the electronegativity of the uppermost atom decreases from O to Te (Fig. 2). We assume that from WSeO to WSeTe, we depict the growth of bacteria, and changing atoms are representing the changing protein structure of the bacterial membrane. We define this change from WSeO to WSeTe in time as cycle 1, and then the cell is growing and the material's atoms are extended upward in the z-direction, which we call it as the second cycle, and so on, as shown in Fig. 3, but we examine only the first cycle in this paper.

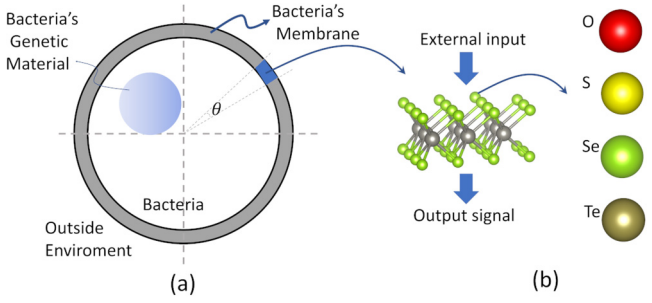

FIG. 1. (a) A cartoon representing the cross-sectional view of bacteria's cell and their membranes and (b) visualization of a W based two-faced single layer as a fragment of the bacterial membrane (gray balls are W, red balls are O, yellow balls are S, green balls are Se, brown balls are Te, and bonds are represented as sticks).

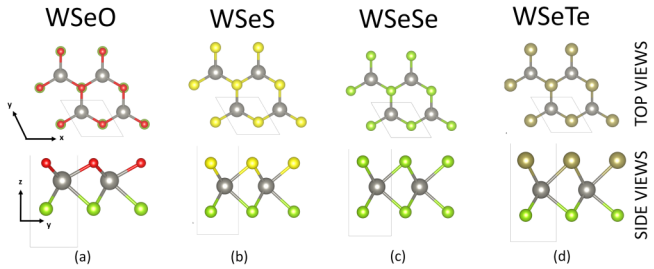

FIG. 2. Top and side views of the tungsten based two-faced single layers: (a) WSeO, (b) WSeS, (c) WSeSe, and (d) WSeTe (gray balls are W, red balls are O, yellow balls are S, green balls are Se, brown balls are Te, and bonds are represented as sticks).

To obtain these single layers, crystal lattice vectors and atomic positional coordinates of the bulk WSeSe are geometrically optimized. Then, a single layer is obtained by a top-down approach. After that, lattice vectors and atomic positions are optimized as explained in Sec. II. Optimized bond lengths of each two-sided single layers are given in Table I. If we sum the bond lengths for each single layer, we conclude that the longest total bond length is found in WSeTe. On the other hand, we measure the thickness of these single layers, which are depicted in Table III, and WSeTe has the highest thickness. Then, we calculate the ratio of the total bond length over thickness, we conclude that only WSeO yields a different ratio, which is roughly 5% higher than WSeTe's ratio. The thickness is the bacterial membrane, and the total bond length is the distance to be traveled by the charged species during the operation. We can consider this longness of the path compared to the thickness as the dominance of the inductive effects in WSeO by inspiring from basic electrical circuits.

First cycle element's electronic band structures are presented in Figs. 4(a)–4(d). We deduce the KS bandgap of each single layer. The highest is found for WSeS, and the lowest is found for WSeO. Among these single layers, only WSeO exhibits an indirect KS bandgap from the K to G point, and other single layers have a direct KS bandgap at the K point. When we consider the band structure of WSeO and WSeTe single layers at the G point, we conclude that two DFT bands with the highest negative energy below the Fermi energy level are splitted more compared to WSeS and WSeSe single layers. In Fig. 4(a), the uppermost DFT energy band below the Fermi energy level is much more flat compared to the other single layers. This may indicate localized states, which may affect the polarization and conductivity of WSeO. We also obtain the Wannier interpolated bands, and these are depicted with dashed red lines in Figs. 4(a)–4(d). We wannierize 13 bands for all single layers except for the WSeTe single layer. For WSeTe, we wannierize 14 bands by additionally considering the tungsten's s orbital because the additionally wannierized band above the Fermi energy level is in interaction with an other band at the K point. We also detect a singularity like sharp peak in the density of states plot in Fig. 4(e), which may correspond to the uppermost DFT energy band below the Fermi energy level of WSeO.

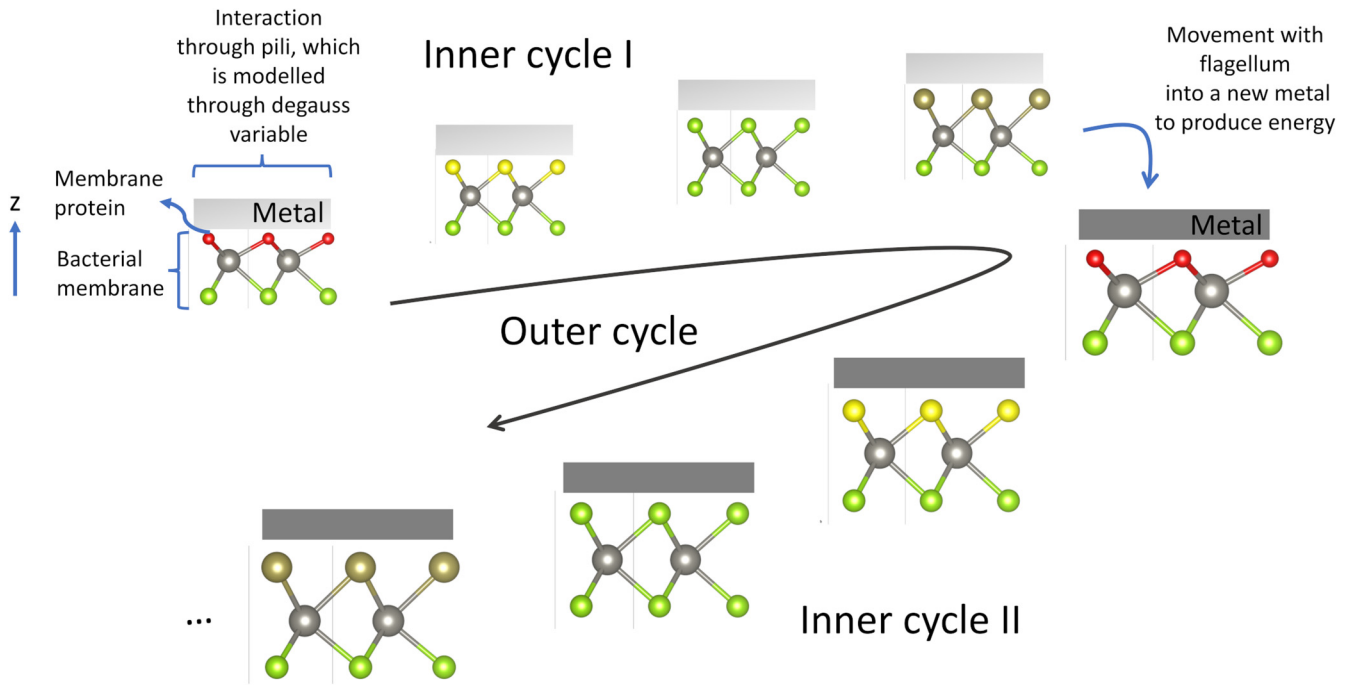

FIG. 3. A cartoon representing the cross-sectional view of a bacterial membrane with tungsten based two-faced single layers, which are changing from WSeO to WSeTe in inner cycle I. Uppermost O, S, Se, and Te represent the membrane protein's different configurations. The metal layer, where the bacterial membrane interacts through its pili, and this metal layer changes in every cycle because bacteria move to other metals with its flagellum. The overall life cycle of the bacteria is called as an outer cycle. Single layers in inner cycle II are given for representative purposes to show the growth and does not correspond to the actual ones.

Finding the electronic structure of each single layer is important because there are voltage-gated K^+ channels in bacteria, which are mainly responsible for the membrane potential variations.

Finding and governing this membrane potential has a key role in the bacterial proliferation and ATP synthesis; for instance, in the case of destruction of a bacterial wall, which may serve as a membrane, bacteria may not be alive.[34–36] In this way, we examine the membrane potential of the single layers, which can be modeled as a capacitor initially by considering the sensory behavior of the bacterial membrane and its dielectric characteristics. The induced maximal transmembrane potential, $\psi_{\max}$, which can be called as membrane potential due to atomic thinness of 2D materials, is given by Eq. (1),

$$\varepsilon_o \psi_{\max} = \frac{3a\varepsilon_o \mathscr{E}}{2\sqrt{1+(2\pi f \tau)^2}}, \tag{1}$$

where a is the radius, τ is the relaxation time, and $\mathscr{E}$ is the electric field strength found from the Berry phase theory of polarization and Eq. (3), which will be discussed later.[37] We investigate the surface potential of single layers vs change in the thickness in the z-direction as shown in Fig. 5(a) by considering the growth as an external trigger.

Semiconductors are dielectric media. When we go from WeSeO to WSeTe, an increase in the macroscopic dielectric constant is observed as given in Table III. Increasing dielectric constant leads to an increasing capacitance based on $C = \varepsilon_o \varepsilon_r (A/d)$, where V is the electric potential, C is the capacitance, Q is the charge, A is the cross-sectional area, and d is the distance. On the other hand, the thickness is increasing from WeSeO to WSeTe. Hence, a definitive comparison in this picture is hard. Therefore, we consider the link between capacity and polarization, P, of a capacitor. In this way, we first write $C = \Delta Q/\Delta V$, and the electric displacement field, $\mathbf{D}$, is written as $\nabla.\mathbf{D} = Q/A$, where we took $\mathbf{D}$ as equal to $\mathbf{P}$. Then, capacitance is given by Eq. (2),

TABLE I. Bond lengths of W–O, W–Se, W–S, W–Te, and the angle between Se–W–O, Se–W–S, Se–W–Se, and Se–W–Te in tungsten based two-faced single layers of WSeO, WSeS, WSeSe, and WSeTe. Lengths are in the units of angstrom and the angle in the units of degree.

	W–O	W–Se	W–S	W–Te	Angle
WSeO	2.10	2.50	…	…	77.64
WSeS	…	2.54	2.42	…	81.67
WSeSe	…	2.54	…	…	82.40
WSeTe	…	2.56	…	2.73	82.62

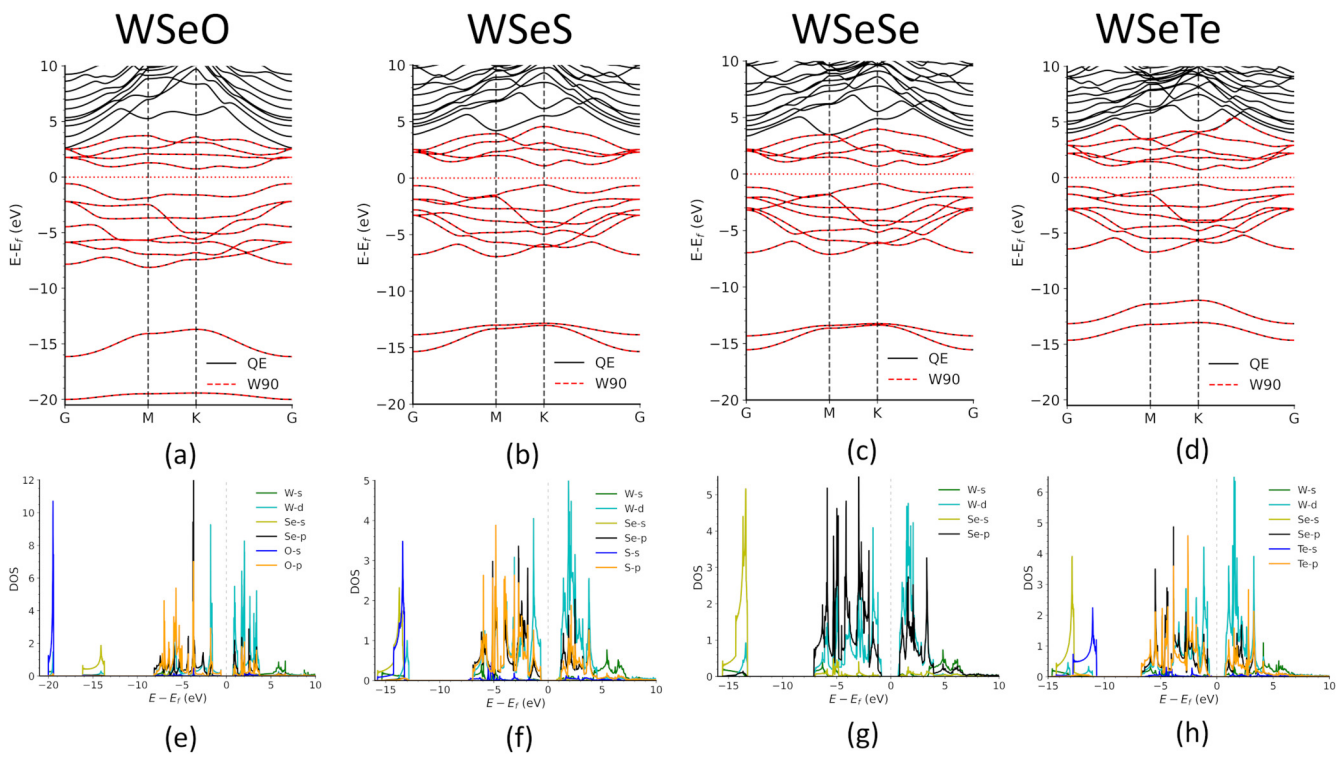

FIG. 4. Electronic band structure based on the PBE functional is labeled as QE, and its Wannier interpolated bands are labeled as W90 for single layers of (a) WSeO, (b) WSeS, (c) WSeSe, and (d) WSeTe; projected density of states (number of states/energy/volume) of (e) WSeO, (f) WSeS, (g) WSeSe, and (h) WSeTe.

$$C = A\frac{\Delta P}{\Delta V}. \tag{2}$$

When we compare Figs. 5(a) and 5(c), it is clear that the potential change is bigger than the polarization change when we go from WSeO to WSeTe. Therefore, capacitance will decrease through WSeTe. Potential and polarization are increasing with an increase in the overall thickness as shown in Fig. 5(a), which are drawn by taking f in Eq. (1) as equal to 0. The variation of the surface potential with frequency is depicted in Fig. 5(b) by considering Eq. (1), where the relaxation time is taken as 1 s for simplicity of the representation. Here, we observe charging of a capacitor with electrons when we consider time as the inverse of frequency in Fig. 5(b). This frequency interpretation will be significant when we begin to discuss about the memristive properties of single layers, like which memory element is dominant in which single layer. For example, memcapacitive behavior will be dominant in WSeTe, even though memcapacitor is not a capacitor.

B. Berry phase theory of polarization

We model the bacterial learning and memory abilities using two-dimensional single layers through biomimicking. The aim of this modeling is to enable researchers to introduce bacterial learning and memory into their robust and high-performance CMOS based devices. This means that we need to stick to macroscopic quantities to model the bacterial learning and memory abilities. We picked WSeO, WSeS, WSeSe, and WSeTe single layers, where O, S, Se, and Te represent proteins. These proteins might be assumed as the different configurations of the same protein. Specifically, the unfolded one is the WSeO, the folded one is the WSeSe, and the aggregated one is the WSeTe based on their entropy because the unfolded one has the lowest entropy and the folded one has the highest entropy. Then, we assume that WSeTe represents the protein aggregation because WSeTe has higher entropy than WSeO. Here, entropy is taken as the overall system's measure of disorder. These kinds of changes in the protein's structure are linked with the hydrogen bonds mostly. The single hydrogen bond dynamics are investigated in the Appendix through numerical methods, where we observe time-varying polarization.

We try to establish a model to depict cycle I as a system. This system is a bacterial membrane, and it is representing the bacteria itself because the bacteria's surface to volume ratio is high. Therefore, by inspiring from the mass conservation, we equate two different polarization equations into each other to find the governing equation of the model. First, we write polarization as a function of electric field because polarization vs electric field relation in Fig. 5(d) exhibits a

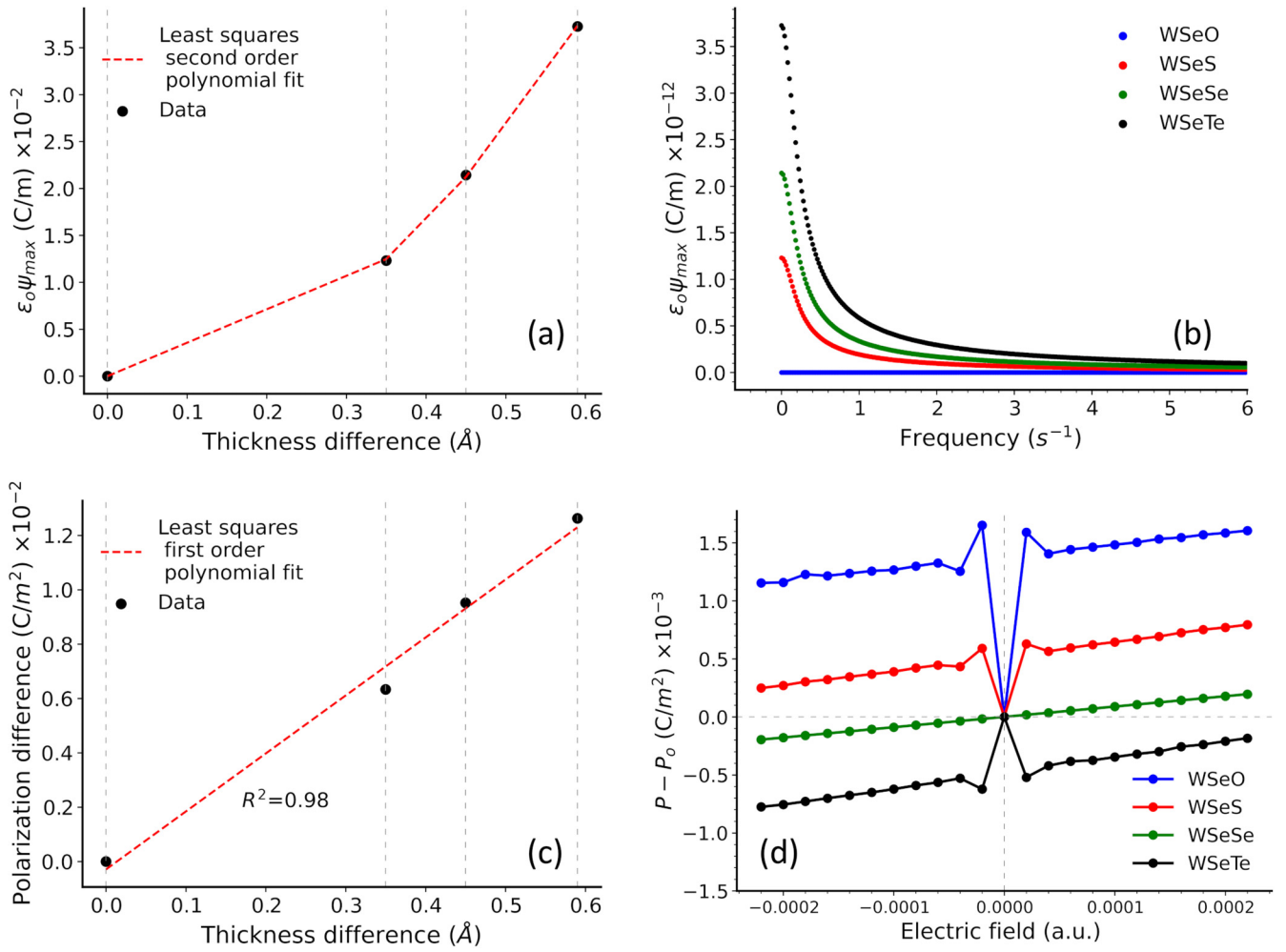

FIG. 5. (a) Surface potential vs thickness difference at zero frequency exhibits a parabolic relation, (b) surface potential vs frequency relation for each single layer, (c) polarization difference vs thickness difference exhibits a linear relation (WSeO's thickness and polarization are taken as a reference, and other single-layer thickness and polarization values are subtracted; the results belong to the 0.005 *degauss* value), and (d) polarization difference vs the electric field plot showing a linear relation.

linear relation. Therefore, polarization, P, can be given by Eq. (3),

$$\mathscr{E} = \frac{P}{\chi \varepsilon_o}, \tag{3}$$

where χ is the electric susceptibility, which is equal to $\varepsilon_r - 1$, where ε_r is the dielectric constant and ε_o is the vacuum permittivity. On the other hand, we observe the relation between the polarization difference and the thickness of single layers as shown in Fig. 5(c), where the polarization is calculated from Eq. (3). This may allow us to write another relation for polarization; namely, the polarization density difference, as given in Eq. (4),

$$P = z\bar{\varepsilon}\bar{E}, \tag{4}$$

where z is the piezoelectric coefficient, $\bar{\varepsilon}$ is the strain, and $\bar{E}$ is Young's modulus. We plug P in Eq. (4) into Eq. (3) and differentiate $\mathscr{E}$ with respect to time by assuming time dependency of $\bar{\varepsilon}$ and χ. Hence, derivative of $\mathscr{E}$ with respect to time can be given by Eq. (5),

$$\dot{\mathscr{E}}(t) = \frac{z\bar{E}}{\varepsilon_o \chi}\left(\dot{\bar{\varepsilon}} - \frac{\bar{\varepsilon}\dot{\chi}}{\chi}\right). \tag{5}$$

We believe that polarization density, dielectric constant, and electric

field are related to each other as a system. The governing equation of the model is depicted in Eq. (5), while bacteria's membrane is coupled to the environment. We believe that this type of modeling does not reflect the whole characteristics of a quantum system because we assume a linear system, even though we believe that this system is non-linear and time-dependent.[38] Nonetheless, this leads to a simple relation, but non-linearity and time dependence will be introduced later to depict each single layer.

Polarization values in the z-direction are obtained using the Berry phase theory of polarization and given in Table III for each single layer. In this calculations, the absolute value of polarization, P_a, for each case is given with modulo per polarization quantum, P_q, which is equal to eR/Ω, where e is the electric charge, R is the lattice vector, and Ω is the volume. For polarization calculations, P is congruent to P_a with y modulus of congruence, $P = P_a \pmod{y}$, where y is a decimal number. Hence, $P - P_a = yn$ for some n, where $n \in \mathbb{Z}$. During our work, we took n as equal to zero. Moreover, the electronic contribution to the polarization is related to the variations in the wavefunctions[39] based on Eq. (6),

$$\mathbf{P}_e = -\frac{2|e|i}{(2\pi)^3}\int_A d\mathbf{k}_\perp \sum_{n=1}^{M}\int_0^{G_\parallel}\left\langle u_{\mathbf{k},n}\frac{\partial}{\partial k_\parallel}|u_{\mathbf{k},n}\right\rangle dk_\parallel, \tag{6}$$

where M is the total occupied number of occupied bands, $k_\parallel$ is parallel to the polarization direction, G is the reciprocal lattice vector, and $|u_{\mathbf{k},n}$ are the states, which can be depicted by Bloch's theorem as $\psi_{\mathbf{k},n}(\mathbf{r}) = u_{\mathbf{k},n}(\mathbf{r})e^{i\mathbf{k}.\mathbf{r}}$. The total DFT energy obtained from KS DFT calculations is a function of the electron density and related to the wavefunction of the material. We also calculate the polarization response in time under a positive valued electric field in the z-direction, and they are depicted in Fig. 13(a). We observe the lowest polarization value in WSeO in its first peak, and this is reasonable when we consider $P = P_{w/o} + \varepsilon_o\chi\mathscr{E}$, where $P_{w/o}$ represents the polarization without an electric field. Since the $P_{w/o}$ value is the highest negative in WSeO, it is reasonable to have the lowest polarization. However, polarization of a WSeSe single layer is found higher than WSeTe, even though WSeTe has a higher positive $P_{w/o}$ value than WSeSe. This can be interpreted with the low dielectric constant of the WSeTe as given in Table III.

To explain the reasons between the difference in polarization values of the single layers, we carry out various analyses. These are Bader charge analysis, COHP, and phonon dispersion. The Bader charge analysis for each atom in single layers is given in Table II, which represents the transferred charges. Specifically, O in WSeO receives a $-1.08e$ charge, which leads to the lowest bond length and the lowest thickness among single layers. The difference between the received charges of O and Se in WSeO may explain why we have the highest polarization compared to other single layers. For example, WSeTe's polarization is positive valued because the difference between the received charges of Te and Se is positive. The number of received charges by each uppermost atom positively correlates with the electronegativities of the atoms. When we consider the electronegativity difference between Te and Se as given in Table II, we conclude that this difference is the reason why W in WSeTe gives away the lowest amount of charge compared to other single layers. Another important difference in Bader analysis is about the received electron difference between O and Se; specifically, O gets more electron than Se. This will lead to larger electrostatic potential energy at the O side; therefore, a larger work function compared to the Se side in WSeO can be seen in Fig. 20(c1). This charge difference may induce the so-called built-in voltage, which scales with the dipole moment of the layers. This is larger in WSeO compared to other layers. In DFT studies of 2D materials with a supercell approach, the effect of this dipole may induce an artificial electric field. To cancel the effects of this artificial electric field, a dipole correction is implemented.[40] However, in this comparative study, we avoid to use dipole correction because the induced dipole is not profound except for WSeO. Moreover, we assume that this dipole is a good representation of the interaction between the substrate and 2D materials since the electric field due to the substrate scales with the dipole of the single layers. Moreover, since the bacteria live in an aquatic environment, a solvent must encapsulate the single layers, which is most of the time modeled as an additional electric field term in DFT.

Polarization of single layers is tried to be analyzed using a projected COHP method. Here, we consider the variations in the crystal orbital Hamilton populations of WSeO's O–W and Se–W bonds, WSeS's S–W and Se–W bonds, WSeSe's upper and lower Se–W bonds, and WSeTe's Te–W and Se–W bonds with respect to the energy. This analysis is important because negative -pCOHP values indicate antibonding states and positive -pCOHP values indicate bonding states. We know that the Berry phase theory of polarization is applied to insulators; in this case, we need to consider the fully filled states. When we consider the negative values of the $E - E_f$, a dip in the O–W bond's plot and a relatively small dip in Se–W bond's plot are observed in Fig. 6(a). We believe that this COHP difference between the O–W and Se–W bonds may be used to explain the polarization of single layers. For example, in Fig. 6(c), these two dips are equal, and polarization calculated from the Berry phase theory of polarization is zero. In Fig. 6(d), the polarization calculated from the Berry phase theory of polarization is positive, which is in line with our argument.

We calculate phonon dispersion relations as shown in Figs. 7(a)–7(d), where phonon dispersions reveal imaginary frequencies, represented as negative in the plots, near the G point for WSeO, WSeS, and WSeTe, which may indicate the dynamic instability of the structures possibly formed due to polar instabilities. The difference in the span of imaginary frequencies near the Gamma point between WSeS and WSeTe can be explained by the increased atomic mass of the uppermost atom from WSeS to WSeTe. The highest observed phonon dispersion frequency is

TABLE II. Bader charge analysis results for the tungsten based two-faced single layers of WSeO, WSeS, WSeSe, and WSeTe. Charges are in the units of elementary charge (e).

	W	O	Se	S	Te
WSeO	1.57	−1.08	−0.49	…	
WSeS	1.22	…	−0.52	−0.70	…
WSeSe	1.09	…	−0.54 and −0.54		
WSeTe	0.88	…	−0.57	…	−0.30

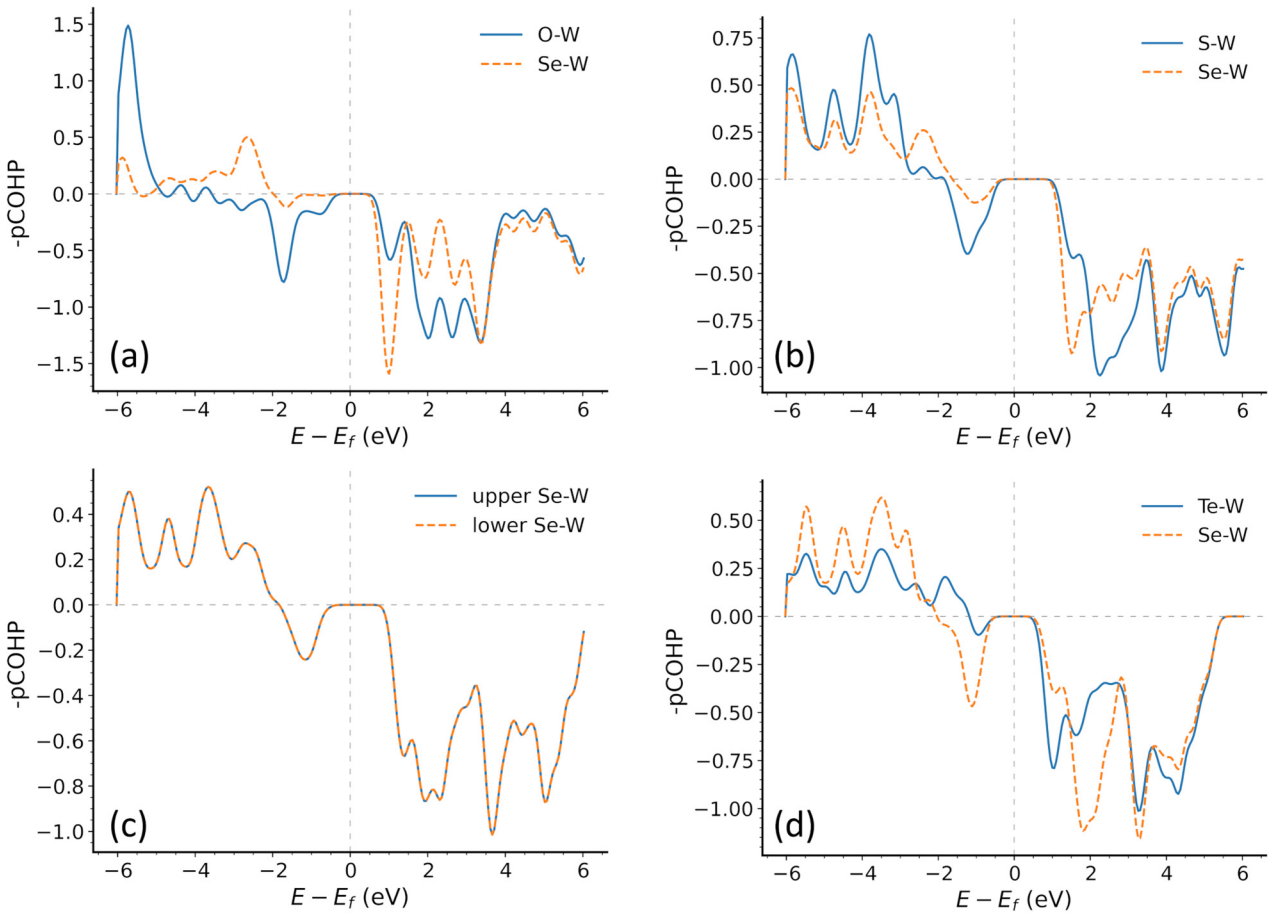

FIG. 6. Projected crystal orbital Hamilton population analysis results for (a) WSeO's O–W and Se–W bonds, (b) WSeS's S–W and Se–W bonds, (c) WSeSe's upper and lower Se–W bonds with respect to the *z*-axis, and (d) WSeTe's Te–W and Se–W bonds.

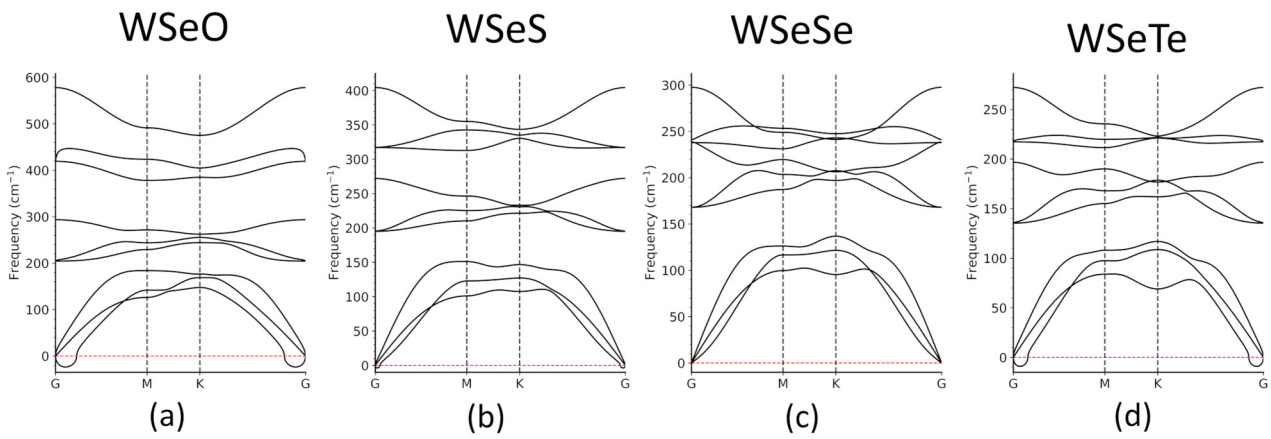

FIG. 7. Phonon dispersions of (a) single-layer WSeO (shows imaginary frequencies near the Gamma point), (b) single-layer WSeS (shows imaginary frequencies near the Gamma point), (c) single-layer WSeSe, and (d) single-layer WSeTe (shows imaginary frequencies near the Gamma point).

TABLE III. Electronegativities of O, S, Se, and Te in the Pauli scale, radius of O, S, Se, and Te, lattice constants, thickness of single layers (SLs), averaged Poisson ratio, averaged Young's modulus, absolute polarization density in the z-direction, out-of-plane macroscopic dielectric constant of the supercell in the Cartesian coordinates (ε_r), total DFT energy, and Kohn–Sham (KS) bandgaps of tungsten based two-faced single layers of WSeO, WSeS, WSeSe, and WSeTe.

	WSeO	WSeS	WSeSe	WSeTe
Electronegativity (Pauli scale)	3.44	2.58	2.55	2.1
R of the uppermost element (pm)	152	180	190	206
Lattice constant (Å)	3.06	3.25	3.32	3.44
SL thickness (Å)	2.90	3.25	3.35	3.49
Poisson ratio	0.216	0.195	0.217	0.189
Young's modulus (kbar)	170.64	126.33	119.91	97.81
Polarization ($\mu C/cm^2$)	−0.952	−0.319	0	0.311
Dielectric constant	1.227	1.274	1.300	1.301
Total DFT energy (Ry)	−427.32	−416.40	−636.77	−603.95
KS bandgap (eV)	1.32	1.69	1.54	1.34

decreased from WSeO to WSeTe, and this is in a positive correlation with the electronegativities of the uppermost atoms. We observe splitting between the fourth uppermost and third uppermost DFT phonon dispersion bands in terms of frequency; for example, WSeO is splitted more compared to others, and WSeSe's phonon bands are not splitted, like in non-polar materials. This splitting of DFT phonon bands is correlated with the magnitude polarization of the single layers. Furthermore, we analyze the speed of sound, V_s, which can be found from the slope of longitudinal acoustic modes near the Gamma point. We compare V_s of single layers with a comparison operator as WSeO>WSeS>WSeSe>WSeTe. This relation found from phonon dispersion is verified by finding Young's modulus values of the single layers with a thermo_pw module. As it is given in Table III, Young's modulus of single layers is positively correlated with V_s because $V_s = (\bar{E}/\rho)^{1/2}$, where ρ is the density.

It is known that bulk conductivity of a material is different from its atomically thin single layer. This difference is because of the size of the material; specifically, we need to consider the scattering effects at the surfaces and reflectivity to calculate resistivity at low dimensions.[41] In this way, Fuchs and Sondheimer formula can be used as given in Eq. (7),

$$\sigma_{FS} = \sigma_{bulk}\frac{3k}{4}\frac{1+p}{1-p}ln(k^{-1}), \tag{7}$$

where σ is the conductivity, k is equal to t/l_o and $k << 1$, l_o is the bulk mean free path, t is the thickness, and p is the reflection coefficient, even though it is defined for metal wires. The p term in Eq. (7) is a function of polarization because decreasing polarization means a decreasing refractive index of the material, thereby decreasing reflectivity. Since we derived all two-sided single layers from bulk WSeSe, we can consider the highest conductivity in WSeO because of its large polarization. The highest conductivity is also visible from a macroscopic perspective because of the lowest bandgap of WSeO among single layers. These variations in conductivity patterns can also be explained by using quantum mechanics. Specifically, we can interpret the high conductivity of WSeO as a positive quantum correction to conductivity, which occurs in long-range scattering potentials, where backscattering is negligible and dephasing may be observed compared to short-range scattering potentials. If we consider this as a positive correction to conductivity, we may consider dephasing, which may indicate the absence of coherency.[42] Based on this conclusion, we can argue more about the characteristics of the system because it is known that loss of coherency is necessary to observe classical memristive characteristics in a quantum memristor system.[43] Therefore, we develop a model inspired from the dynamics of a quantum memristor.

C. A time-functional pseudo-quantum memory element

We model the dynamics of bacterial learning and memory in a system composed of unit cells of WSeO, WSeS, WSeSe, and WSeTe single layers, which are shown in Fig. 3 as the inner cycle I. Each of these unit cells includes the fully relaxed KS DFT configuration of single layers. These single layers represent the bacterial membrane, and O, S, Se, and Te atoms represent the membrane protein. We design a DFT simulation protocol and a model by inspiring from bacteria living in water, that is, *Geobacter metallireducens*. It does not use oxygen to generate energy, but it can generate energy by using electrical current through its pili, which are hairy extensions as shown in Fig. 8.[44] This electrical current is because of the interaction between bacteria through its pili and metal. We try to mimic this interaction between the dielectric medium and the metal because we treat the bacterial membrane as a dielectric medium.

Bacteria live together, and they rub each other through their membranes as shown in Fig. 9(a). These membranes are dielectric media. This means that they can be charged after rubbing each other. We first consider WSeS, where the bacterial membrane is negatively charged similar to the human neurons. In WSeTe, this initial charge might be positive. This negatively charged membrane is analog to the $+V$ applied material as shown in Fig. 9(b). As shown in line 1 of Fig. 11(d), this corresponds to an increase in polarization. Then, it begins to contact to a charge neutral metal as shown in Fig. 9(c). Therefore, insulator's electrons are transferred to metal, and this case is similar like applying $-V$ to the bacterial

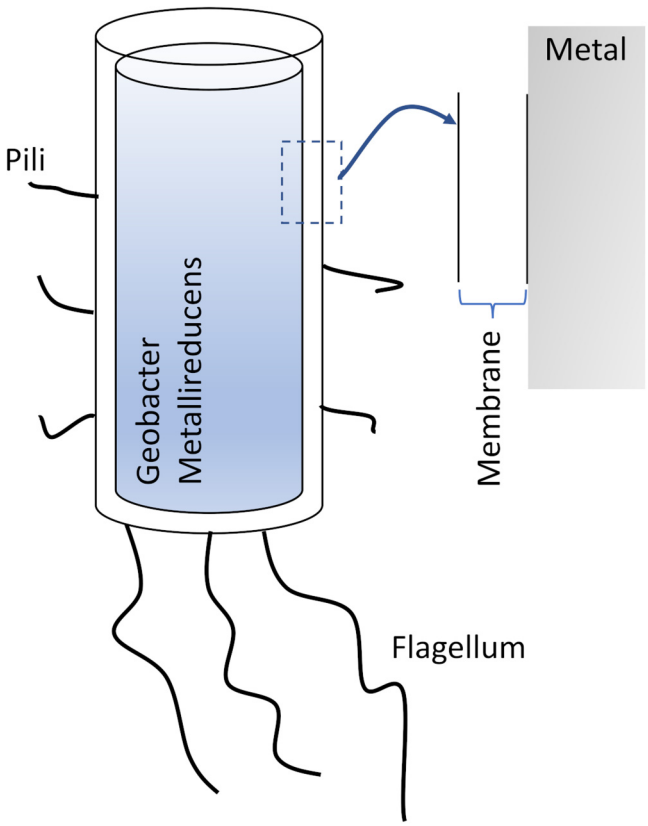

FIG. 8. Cartoons representing the bacteria *Geobacter metallireducens* with its pili and flagellum, which are hairy extensions, charge dynamics between the bacterial membrane and metal through an electron transfer. Bacteria can generate energy by using electrical current.

membrane, which corresponds to line 2 in Fig. 11(d), even though we depict the bacterial membrane as it is in contact with metal. This membrane is using its pili structure to generate this electrostatic interactions. Most probably, pilis on the surface of bacteria are developed to increase the charge transfer by creating high electric field strength.

We assume that these new charges in the metal will arrange itself as negative charges far away from the bacterial membrane. In this configuration, the bacterial membrane and the metal will repel each other. When they are separated, they will lose charge to the outside environment since this is an open system. It is known that the charges in a dielectric medium can only spread into small areas on its surface. We can conclude that it is easier to remove electrons from a dielectric medium than a metal. Therefore, more negative charges are given to the environment by the bacterial membrane compared to the metal as shown in Fig. 9(c) because decreasing the *degauss* value indicates decreasing electronic temperature and conductivity decreases for a semiconductor; on the other hand, a metal is a good conductor almost at all temperatures. This follows an attractive interaction between the bacterial membrane and the

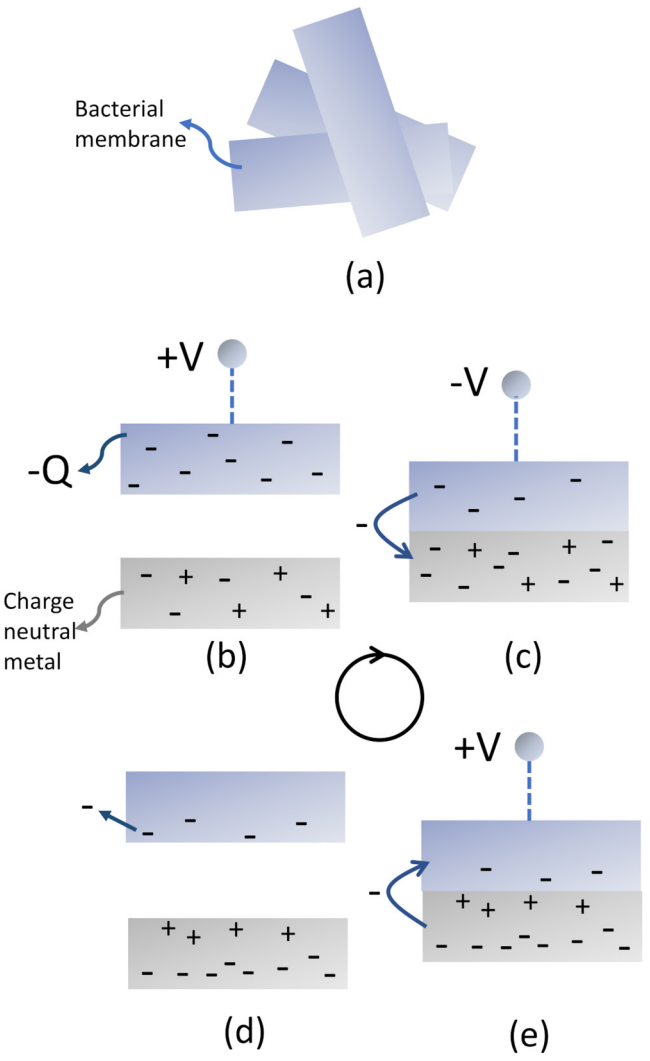

FIG. 9. Modeling of possible electrostatic interactions between the metal and bacterial membrane: (a) Bacterial membranes interact through rubbing, (b) the bacterial membrane is negatively charged, like in the case of WSeS, (c) charge transfer from the bacterial membrane to metal, (d) loss of charge in the bacterial membrane, and (e) a charge transfer from a metal to bacterial membrane.

metal because of the Coulomb interaction between charged species, which scales with the inverse square of the distance between the charges. When they are in contact as shown in Fig. 9(e), a charge transfer from a metal to a bacterial membrane may occur, which corresponds to line 3 in Fig. 11(d). This corresponds to applying a $+V$. Then, they repel each other again like repelling of two charged species with the same polarity. After that, the bacterial membrane loses more charge than the metal similar to a phenomenon depicted in Fig. 9(d). This is like a $-V$ applied to the bacterial membrane, which corresponds to line 4 in Fig. 11(d). This process is repeating itself with line 5 in Fig. 11.

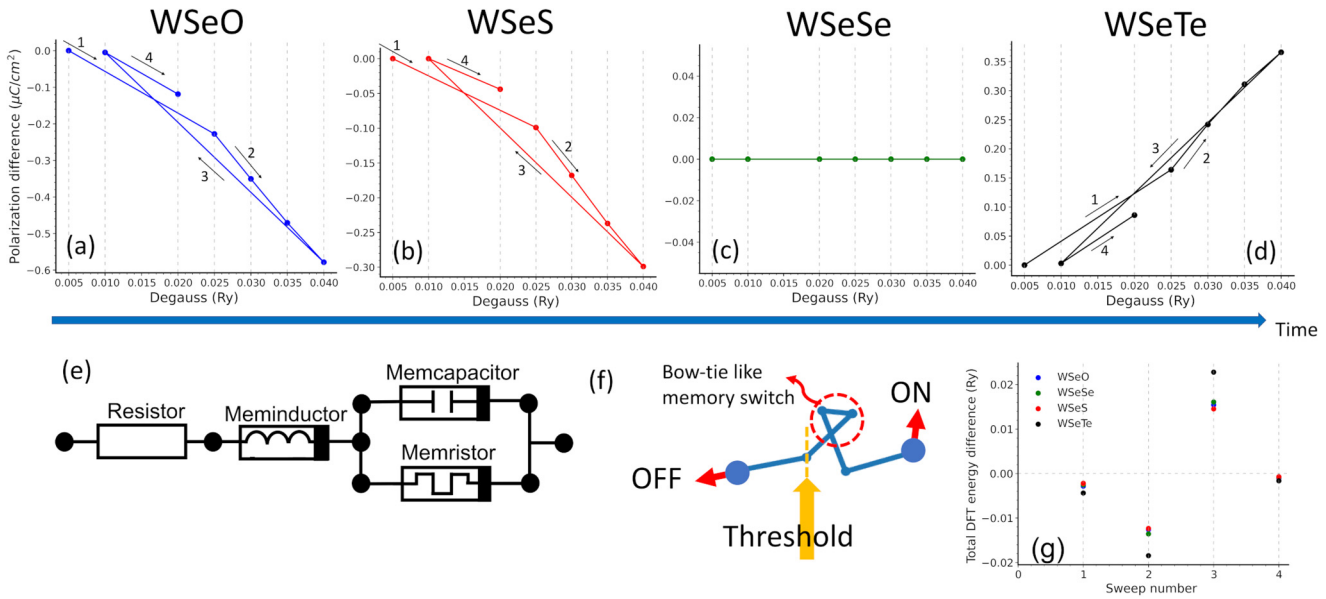

FIG. 10. (a) Polarization difference vs the *degauss* plot with its bow-tie memory switches after the respective thresholds for WSeO, (b) the polarization difference vs *degauss* plot with its bow-tie memory switches after the respective thresholds for WSeS, (c) the polarization difference vs the *degauss* plot for WSeSe, (d) the polarization difference vs the *degauss* plot with its bow-tie memory switches after the respective thresholds for WSeTe, (e) modeling of the proposed system with resistor, memcapacitor, memristor, and meminductor, (f) conventions and standards of the ON and OFF read points for the memory switch, and (g) the total DFT energy difference for each sweep numbers for all single layers.

We try to model the non-linear and time-dependent interactions between the bacterial membrane and the metal through biomimicking and also by inspiring from proteins, which are composed of amino acids. These may have negative charges, but they cannot repel each other because they are bound to backbone with the covalent bond. They will have a tendency to get positive charges from the outside environment. This means that each of the time the protein conformation changes. We simulate this metal and bacterial membrane interaction model depicted above using DFT because bacterial learning and memory cannot be explained without quantum mechanics. In this way, we introduce the *degauss* parameter of Quantum ESPRESSO, which will allow us to quantize the macroscopic physical quantities in DFT simulations, such as charges. *Degauss* is the electronic temperature, and it governs the occupation numbers's broadening around the Fermi energy level. It has a relation with smearing; specifically, *degauss* can be regarded as a magnitude of smearing, where smearing is a distribution function for occupations of DFT bands.[45]

As it can be seen from Fig. 10, the *degauss* value is first increased and then decreased; while doing this, we record the polarization. We consider that *degauss* is like a time-varying oscillatory electric field because *degauss* changes the Fermi energy level of the material in the unit cell, which can be regarded as an additional charge or depletion of charge as shown in Fig. 10(a). In our simulation, we also see that polarization changes its direction with *degauss* in a polar crystal, such as WSeS. This is very similar to a ferroelectric ceramic $BaTiO_3$, where the crystal transforms from cubic to tetragonal when we increase the temperature; this means that it is a displaced Ti^{4+} atom. The energy profile of Ti^{4+} with respect to the position is very similar to the potential depicting a hydrogen bond, which is like a double-well potential. Hence, an electric field in the opposite direction can cause Ti ions to displace from one well to other. Therefore, the dipole moment can be reversed, like in our case. We may simulate a change in the direction of the spontaneous polarization with the *degauss* parameter. In our model, the interaction between the metal and insulator is to enable them to be simulated with the *degauss* parameter, which indeed simulates the time-dependent oscillating electric field.

The *degauss* parameter has to be converged in a DFT calculation; however, when we choose smearing as the Fermi–Dirac distribution function, we can consider the *degauss* value as a parameter representing the electronic temperature. The *degauss* value, which has a unit of energy, represents how large the smearing is. This smearing value is indeed used for metals to locate the Fermi level. Here, we have semiconductors. Therefore, the Fermi level found after the calculation is not the exact Fermi level defined for metals, but it might be regarded as a quasi-Fermi level. Polarization difference values corresponding to each *degauss* value are depicted in Figs. 10(a)–10(d), where the *degauss* value is interpreted as the shift of the Fermi energy level with respect to a reference vacuum level, and this is similar to adding or subtracting a charge to a unit cell. For example, if we add positive charges to the unit cell, then the Fermi energy level shifts upward with respect to the reference energy level as it is depicted in Fig. 11, where the reference energy level is taken as the maximum vacuum level as calculated in Fig. 20 of the Appendix.

We calculate the electrostatic potential energy variations of single layers with respect to the z-direction in the unit cell. We use the maximum of this energy as the reference energy level, and we subtract this energy from the Fermi energy level, which is read from the self-consistent field calculations. We report this difference, PE-E_f, in Figs. 20(a1), 20(b1), 20(c1), and 20(d1) for each single layer. Their enlarged figures are shown in Figs. 20(a2), 20(b2), 20(c2), 20(d2), 20(b3), 20(c3), and 20(d3). For example, in WSeSe, both Fermi level and the vacuum level are positive valued. In Fig. 20(b), the potential energy difference from the Fermi level, PE-E_f, is given for WSeSe. The difference increases from 0.005 to 0.025 Ry; therefore, the Fermi level decreases from 0.005 to 0.025 Ry. This will be interpreted as an addition of charge, $-Q$, into the unit cell, namely, a positive valued voltage. Then, PE-E_f decreases up to 0.04 Ry as shown in Fig. 20(b); therefore, the Fermi level increases up to 0.04 Ry. This means an addition of positive charge, $+Q$, namely, a negative valued voltage for WSeSe.

In WSeS, vacuum levels are positive valued and the Fermi level is negative valued. In Fig. 20(b1), we represent the PE-E_f vs distance plot for WSeS. We consider the vacuum level as the maximum of this plot; namely, the plateau located at the right-hand side in Fig. 20(b3). This means that when PE-E_f increases up to 0.02 Ry, the Fermi level decreases. This might be considered an addition of a negative valued charge into the unit cell, namely, a positive valued voltage. After this, the Fermi level increases up to 0.04 Ry for WSeS. In Fig. 20(c1), PE-E_f vs distance plot for WSeO is given. We consider the vacuum level as the maximum of this plot, namely, the plateau located at the right-hand side as shown in Fig. 20(c3). Here, vacuum levels are positive valued for all *degauss* values, and the Fermi level is negative valued as in the case of WSeS. We observe that PE-E_f decreases from 0.005 to 0.04 Ry for WSeO; this might be considered an addition of a positive valued charge into the unit cell, namely, a negative valued voltage. Finally, PE-E_f vs distance plot is depicted in Fig. 20(d1) for WSeTe. We consider the vacuum level as the maximum of this plot; namely, the plateau located at the left hand side of Fig. 20(d1). Here, vacuum levels and *degauss* values are positive valued. From 0.005 to 0.04 Ry, PE-E_f usually decreases; the Fermi level goes up from 0.005 to 0.04 Ry for WSeTe. This might be considered an addition of a positive valued charge into the unit cell, namely, a negative valued voltage. This analysis was based on self-consistent field calculations; however, a more accurate discussion might be given by considering the valence band maximum, VBM, and the Fermi energy level difference obtained from NSCF calculations.

We calculate the polarization with respect to *degauss*, and we depict the results in Figs. 10(a), 10(b), and 10(d). This relation will be important when we discuss the memory behavior of a single layer. In WSeS, *degauss* is a parameter and it changes from 0.005 to 0.4 Ry, then from 0.4 to 0.01 Ry , and then from 0.01 to 0.015 Ry as shown in Fig. 10(b). Therefore, first, it must be charged, then it must lose charge, then charged again, and so on. This is depicted in Fig. 11(d) from line number 1 to line number 5 for WSeS. This interaction of bacterial membrane with the metal is simulated by varying the *degauss* parameter of the Quantum ESPRESSO. Figure 11(d) is the polarization difference vs the *degauss* plot belonging to WSeS. Here, we choose a path marked as 1, 2, 3, 4, and 5. Then, we transform Fig. 11(d) into Fig. 11(e) by considering the voltage as proportional to *degauss* and current as proportional to the polarization difference, even though the current not only depends on polarization, which will be discussed later. On the other hand, we transform polarization into current by considering only the contribution of the motion of paired charges, namely, the polarization current in this picture.

Transformation of Fig. 11(d) into Fig. 11(e) can be depicted as follows. Line I in Fig. 11(e) represents the region from 0.005 to 0.02 V in the x axis, and this corresponds to an increase in the voltage because of decreasing Fermi level. In line II, from 0.02 to 0 V, it is like that a negative voltage is applied because the Fermi level is increasing. Line III, from 0 to 0.02 V, represents an increasing voltage due to decreasing Fermi level. The current value in line III is higher than line II. After that, from 0.02 to 0.01 V, current decreases and reaches a value close to zero, which is depicted with line IV. Here, voltage is decreasing because the Fermi level increases from 0.02 to 0.01 V. Finally, in line V, from 0.01 to 0.02 V, current and voltage increase due to decreasing Fermi level. It is clear that the increase in the negative charge in line 1 of Fig. 11(d) leads to increasing polarization. Then, polarization continues to increase as shown in line 2 of Fig. 11(d) due to the decreased distance between the membrane and metal, hence the increased electric field, if we consider these charges are like forming dipoles between the membrane and metal as shown in Fig. 9(c). In Fig. 11(d), line 3 depicts a decrease in polarization due to charge loss, which can occur as depicted in Fig. 9(d). This charge decrease continues in line 4 of Fig. 11(d).

The above model is designed inspired from bacteria called *Geobacter metallireducens*. Its cartoon is depicted in Fig. 8, where the current flows from the metal to bacteria and electrons in the opposite way, which leads to an increase in the bacteria's electron density periodically or the other way round. This electricity generation is periodic; specifically, bacteria can move with its flagellum and find a new host metal to generate this energy. This event is repeating itself as it is pictured in Fig. 3. In our model, we use single layers to mimic this system with nature. Each single layer itself is a quantum subsystem. If we consider these quantum subsystems as a single quantum system, where the single layer is shifting its position repetitively in time. This system can be regarded as a time crystal by definition. This is a very good indication of having a so-called composite quantum system time crystal because in time crystals, energy does not lose and motion occurs without a change in kinetic energy. Moreover, it is known that the generic time crystals may compose the quantum computer memories.[46] However, this is not a single state, and the material is not always in the ground state but with a slight change in the total DFT energy. When we consider the inner cycle I, we have four different quantum subsystems, and a composite system can be established in the following Hilbert space of $H_1 \otimes H_2 \otimes H_3 \otimes H_4$, which is composed of tensor products, $\otimes$, of individual subsystems, which are 1, 2, 3, and 4 representing WSeO, WSeS, WSeSe, and WSeTe. Hence, the state of the composite system can be given by Eq. (8),

$$|\phi\rangle_{1234} = |\phi\rangle_1 \otimes |\phi\rangle_2 \otimes |\phi\rangle_3 \otimes |\phi\rangle_4, \tag{8}$$

where $|\phi\rangle$s represents each subsystem's state.[47] Each subsystem's

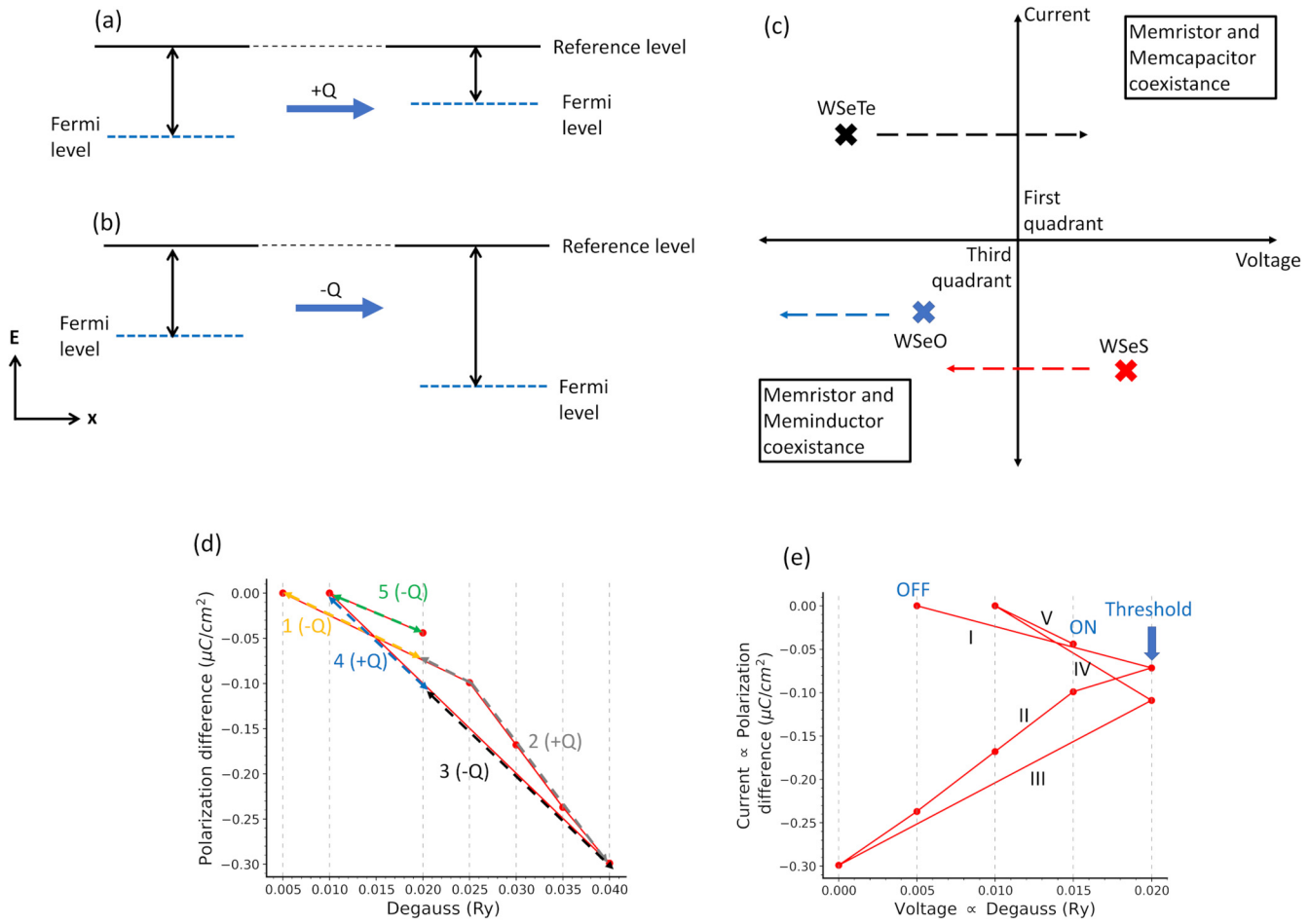

FIG. 11. (a) A cartoon representing the shifting of the Fermi energy level with an addition of $+Q$, (b) shifting of the Fermi energy level with an addition of $-Q$, (c) a cartoon current vs voltage plot, where the crossing at the first quadrant indicates the coexistence of memristor and memcapacitor and crossing at the third quadrant indicates the coexistence of memristor and meminductance, positions of the crossing points are not scaled (d) polarization difference vs the *degauss* plot after the respective thresholds for WSeS, (e) current, taken as proportional to the polarization difference, vs voltage, taken as proportional to *degauss*, plot with its bow-tie memory switches after the respective thresholds for WSeS.

state can be written in terms of its basis sets, which are changing with the modification of the material's lattice vectors.[48]

The learning and memory properties of bacteria can be well described by the quantum properties of materials due to an increased surface area of the bacteria compared to its volume. Furthermore, bacterial learning and memory are believed to be linked with its genome. Therefore, we establish analogies between several concepts and how they conceptually comply with our model during DFT simulations. These concepts are coherence, quantum memristors, measurement-induced phase transitions, gene regulatory network, and so on. Although our system under investigation is neither a spin-qubit nor a superconducting LC circuit. In this way, we consider a property of a quantum memristor, which is that it functions as a classical memristor when coherence is absent.[43]

When we consider each subsystem, it is clear that dephasing is dominant in WSeO when we consider its high conductivity. We can also consider single layers at each distinct *degauss* value as a subsystem of a subsystem in time. We investigate whether this property of the quantum memristor is valid for sweeps inside a single layer. We depict the total DFT energy differences between the beginning and the end of each sweep in Fig. 10(g) because coherent states must satisfy the minimum uncertainty relation given as $\Delta E \Delta t = \hbar^2/4$. In a semi-classical approach, ΔE can be taken as a repetitive increment of the total DFT energy, where $\hbar^2/4$ is 1.083×10^{-31} eVs. We observe that this difference is profound in sweep number 2 and 3, where we end up with different time ranges compared to sweep number 1 and 4. Based on the total DFT energy difference with respect to the sweep number plot in Fig. 10(g), in the second and third sweeps, this coherency is

believed to be diminished, and this is believed to be system's highly conductive parts and also the system is designed to exhibit bow-tie memory switches in these ranges. In these kinds of calculations for coherency, the accuracy and precision of the total DFT energy and energy levels are of utmost importance.

D. System modeling with memory elements: Memristor, meminductor, and memcapacitor

Conversion of a polarization difference vs a *degauss* plot into a IV-like plot is depicted in Figs. 11(d) and 11(e) for WSeS. In a similar manner, we can find the corresponding IV-like plots of other single layers. It is important to determine the IV-like plots of single layers because memory properties are investigated by observing the bow-tie like memory switches. The presence of bow-tie like crossing points in the first quadrant of a Cartesian coordinate in the IV-like plot suggests that the system can be modeled using a memristor and a memcapacitor, and bow-tie like crossing points in the third quadrant suggest that the system can be modeled using a memristor and a meminductor as shown by Qingjiang *et al.*[49] In this way, the crossing point for WSeO is found in the third quadrant, where x is negative and y is negative. WSeS's crossing point is found in the fourth quadrant, where x is positive and y is negative. Finally, the crossing point of WSeTe is found in the second quadrant, where x is negative and y is positive.

In the picture above, we did not consider the built-in voltages. These built-in voltages can be deducted from the electrostatic potential energy analyses as shown in Fig. 20. For example, in WSeTe, it is expected to have a electric field from Te to Se, and this means a positive built-in voltage. On the other hand, this is negative for WSeO and WSeS. We can shift the crossing points based on built-in voltages, and we consider shifting in the positive x direction for WSeTe and shifting in the negative x direction for WSeO and WSeS as shown by the dashed lines in Fig. 11(c). Hence, in WSeTe, th coexistence of memristor and memcapacitance might be considered the most dominant memory element. In WSeO and WSeS, the coexistence of memristor and meminductance might be considered the most dominant memory element as shown in Fig. 11(c).

We conclude the presence of the most dominant memory element by considering J_p as proportional to polarization. Determining IV-like characteristics based on polarization currents may not give the crossing points at the correct polarities for some cases. We may need to shift these current values depending on other contributions to the total current, $\mathbf{J}_{tot}$, like free current, $\mathbf{J}_f$, displacement current, $\mathbf{J}_d$, and magnetization current, $\mathbf{J}_m$, as given by Eq. (9),

$$\mathbf{J}_{tot} = \mathbf{J}_f + \mathbf{J}_d + \mathbf{J}_m, \tag{9}$$

where $\mathbf{J}_f$ is equal to $\sigma\mathbf{E}$, $\mathbf{J}_d$ is equal to $\partial\mathbf{P}/\partial t + \varepsilon_o(\partial\mathbf{E}/\partial t)$, and $\mathbf{J}_m$ is equal to $\nabla \times \mathbf{M}$. In addition to the $\partial\mathbf{P}/\partial t$ term, another moving charge terms might be important. These are $\mathbf{J}_f$ and $\mathbf{J}_m$. We neglect the contribution from magnetization for this part of the calculation, and this will be discussed later. Hence, we consider the $\mathbf{J}_f$ term. For example, when we consider WSeO, which has a high dielectric constant and polarization, polarization current might be dominant for this case. Therefore, its characteristics may appear in the third quadrant as shown in Fig. 11(c). We believe that this shows only the domination of memory elements; therefore, the system can still have other elements. Therefore, our model can exhibit both three fundamental memory elements in time when we consider *degauss* over polarization as proportional to the resistance.

The circuit model based on memory elements is shown in Fig. 10(e) with a load resistor. The memristive effect is investigated further by showing how the frequency affects the IV-like characteristics of the system depicted in Figs. 10(a)–10(d). The effect of frequency can be understood from Fig. 5(b), where increasing frequency leads to decreasing surface potential. Hence, the curves in the *degauss* axis in Fig. 10 will slide to the left, while 0 stays steady. The area will decrease as it is expected in a memristor at high frequencies.[50] Since we consider the change from WSeO to WSeTe as the growth of the bacteria, we believe that after a certain strain, bacteria will divide and this loop will eventually close either at the origin or somewhere, like a time crystal, because time crystals also switch back to its first configuration after some time.

Showing which memory element is dominant in which single layer, namely, in time, is significant. For example, memcapacitive behavior is consistent with the dielectric characteristics of the membrane and with its sensory capability. The desired sensory range is defined as the range, where the output is predictable due to reduced hysteresis, namely, a single value of polarization at a single value of *degauss*. Meminductance is related to the energy generation capability of bacteria, which has been identified as one of the characteristics of bacteria by other researchers; meminductors could potentially be used in the future for self-energy generation devices according to the literature.[51–53] We carry out simulations to understand how well the single layers can mimic the meminductive behavior. Meminductivity can be deduced by observing the hysteresis in current vs magnetic flux plots. Therefore, we try to deduce a current vs magnetic flux like plot belonging to WSeO based on the polarization difference vs the *degauss* plot as shown in Fig. 10(a) and σ_{xx}/τ vs $B\tau$ plot as shown in Fig. 21(a). Here, σ_{xx}/τ vs the $B\tau$ plot for single layers is found from ordinary magnetoresistance calculation. In Figs. 21(a)–21(d), when we consider σ_{xx}/τ vs $B\tau$ plots at a certain $B\tau$ value, it is clear that the σ/τ value varies with temperature. We compare this variation using comparison operators as WSeTe > WSeO > WSeS and WSeSe. We try to estimate current vs a magnetic flux plot by biomimicking. We consider the bacteria *Geobacter metallireducens*, which uses Fe to generate electricity. If a varying current pass through a magnetic material, it can generate a magnetic field. We estimate this magnetic field, B, as proportional to the current from the Ampere–Maxwell equation as given by Eq. (10),

$$\nabla \times \mathbf{B} = \mu_o\mathbf{J} + \mu_o\varepsilon_o\frac{\partial\mathbf{E}}{\partial t}. \tag{10}$$

We consider only polarization current's contribution to the $\mathbf{J}$ term in Eq. (10). Therefore, we consider J_p as proportional to B. We place the red, green, black, and yellow points in the inset of Fig. 12 into the σ_{xx}/τ vs $B\tau$ plot by considering B as proportional to J_p. This will allow us to place these points in the x axis. Since we

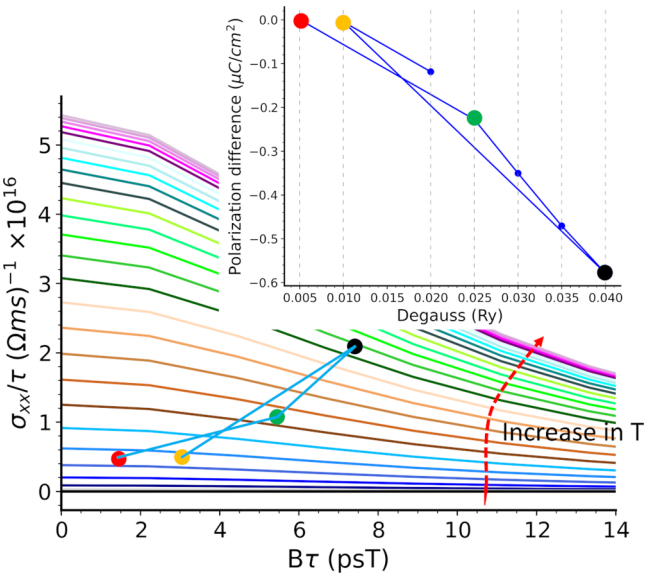

FIG. 12. Ordinary magnetoresistance calculations, σ_{xx}/τ, as a function of the magnitude of magnetic field (B) in the z-direction for different temperatures for tungsten based two-faced single layers of WSeO. The inset shows the polarization difference vs the *degauss* plot for WSeO. The light blue plot is representative and not scaled with respect to the axis, and we expect pinching at the origin.

know the relationship between current and degauss, we can find the corresponding degauss value of the current, which is assumed to correspond to the temperature in σ_{xx}/τ vs $B\tau$ plot as shown in Fig. 21(a). Therefore, the *degauss* value, which is positively correlated to the electronic temperature, will allow us to determine the y-axis position of these points. We place the red, green, black, and yellow points into σ_{xx}/τ vs $B\tau$ plot. We believe that σ_{xx}/τ corresponds to current if we consider a constant applied electric field in magnetoresistive calculations. Hence, σ_{xx}/τ can be considered proportional to current. We also assume the area as constant for each single layer so that we can say that BA is proportional to B. The plot is drawn with light blue lines with the above assumptions qualitatively and is depicted in Fig. 12. It exhibits bow-tie like switching.

We argue that WSeS and WSeO have higher meminductive abilities compared to other single layers based on the locations of the crossing points in their IV-like plot in the Cartesian coordinate system. We compare this result with the meminductance interpretation of single layers revealed from an ordinary magnetoresistance calculation as shown in Fig. 12, where we plot σ/τ vs $B\tau$ relation. There are three points making this comparison hard: the first one is the relaxation time, τ, which may change from material to material, and second, determination of the area to calculate the flux from the $B\tau$ value. When we consider τ as constant for each material and the area scales with the lattice constant, we may end up with the largest variation in the y axis in Fig. 21 in WSeO and WSeTe. Third, we depict σ_{xx}/τ as a function of the magnetic field magnitude times the relaxation time, $B\tau$, in the z-direction for different temperatures. Moreover, in ordinary magnetoresistance calculations, we set the Fermi energy level 0.026 eV above the valence band maximum, VBM, for both single layers. We took the Fermi energy level very close to the VBM; therefore, this conductivity cannot be regarded as intrinsic conductivity. We know that these kinds of simulations by assuming a Fermi energy level and calculating the conductivity based on a single KS DFT band will only give us a qualitative clue about the abilities. Nonetheless, these results, where we suspect from high capability of meminductivity, are in line with the results found in system modeling with the memory elements section for WSeO and for WSeS if we consider the large switching window of WSeS in its polarization vs *degauss* plot compared to WSeTe and the thickness of WSeTe is larger than the WSeS, which might be important because Eq. (10) has a curl of the magnetic field. Moreover, meminductive ability is apparent in WSeO over a wide span of magnetic field values compared to others; for example, the variation of σ/τ with respect to $B\tau$ is apparent only for up to around 10 *psT* in WSeTe.

We observe the response of WSeO to an externally applied electric field through its polarization change with time. These polarization characteristics with time are shown in Fig. 13(a), where the polarization returns approximately to its initial state 0 after a peak. This indicates the high damping factor characteristics of the subsystem WSeO compared to other single layers. We conclude this damping observation by considering an RLC circuit based low-pass filter configuration, which can be seen by modifying the model in Fig. 10(e) with R, L, and C. Even though a memristor is not a resistor, a meminductor is not an inductor, and a memcapacitor is not a capacitor, we consider a resistor and an inductor in series and a capacitor in parallel to a resistor, $R_{load} - L - (R\|C)$, where the total impedance, Z_{tot}, is given by Eq. (11),

$$Z_{tot} = R_{load} + \frac{R}{1 + w^2R^2C^2} + j\frac{wL + w^3LC^2R^2 - wR^2C}{1 + w^2R^2C^2}, \tag{11}$$

where R_{load} is the resistor of the load resistance, R represents the resistor instead of the memristor, C represents the capacitor instead of the memcapacitor, L represents the inductor instead of the meminductor, and w is the frequency. Hence, the damping factor, ζ, of this low-pass filter is given by Eq. (12),

$$\zeta = \frac{1}{2R}\sqrt{\frac{L}{C}}. \tag{12}$$

Equation (12) indicates L > C for WSeO, where the memory characteristics might be dominated by meminductive elements. The dominance of meminductivity in WSeO can be further confirmed by considering the location of crossing points in the IV-like plots as shown in Fig. 11(c), where WSeO's crossing point is located in the third quadrant, which implies the existence of meminductance and memristor.

In Fig. 10(c), we observe the variation of polarization with respect to the *degauss* parameter for WSeSe, even though we believe that the current in WSeSe is mainly due to unpaired charges under an electric field. The *degauss* parameter is used to tune the charge and, therefore, the voltage. If we consider the

charge as a state variable, current can be considered the derivation of charge with respect to time, which corresponds to the y axis in Fig. 10(c). This means that polarization current is almost zero with a varying state variable. In the literature, this behavior is observed in a power-off plot and indicates continuum memory; moreover, a system may exhibit non-volatility at this point.[54]

We use a thermo_pw module and try to generate a relation between entropy and temperature. As expected, entropy increases from WSeO to WSeSe and then decreases from WSeSe to WSeTe, which can be seen in Fig. 13(d) at a constant temperature. In Fig. 13(e), we saw that WSeO is not thermally stable after carrying out *ab initio* molecular dynamics simulations, and this may indicate low entropy of the system. From Fig. 13(d), we consider how big S is at a certain temperature is important to understand and interpret the meminductive behavior of the systems in our approach based on ordinary magnetoresistance calculations. We compare the entropy of single layers from Fig. 13(d) at a constant temperature as WSeSe > WSeTe > WSeS > WSeO. On the other hand, smearing contribution to total DFT energy is found from an electronic temperature times entropy, $-TS$, value through self-consistent field calculations with different *degauss* parameters. The variation of $-TS$ might be linked with *degauss* as shown in Fig. 13(c). It must be noted that these two T and S, which are from self-consistent field calculations and from thermo_pw, are not equivalent by definition.

We estimate how large the variations in $-TS$ within a certain range of degauss values from Fig. 13(c). We compare it as WSeTe > WSeSe > WSeS > WSeO. Therefore, at a certain *degauss* range, the electronic temperature of WSeO and WSeS will vary more compared to other single layers by assuming S from self-consistent field calculations and S from thermo_pw are scaling, even though they are not the same thing. If the variation in the electronic

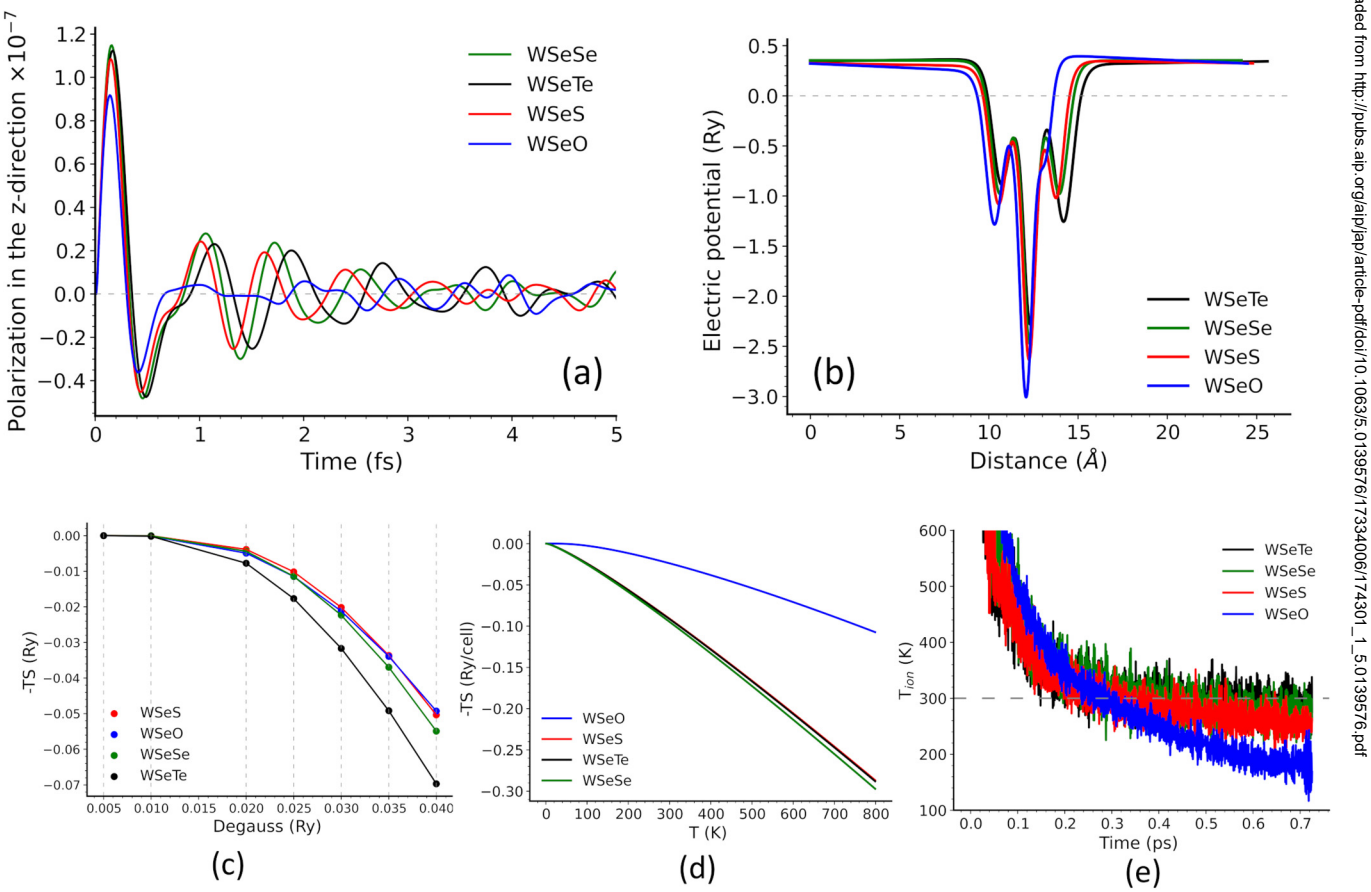

FIG. 13. (a) Real-time linear response (polarization in the z-direction vs time) as a result of an applied positive valued delta function electric field for single layers of WSeO, WSeS, WSeSe, and WSeTe, (b) an electric potential variation in the unit cell for single layers of WSeO, WSeS, WSeSe, and WSeTe, (c) temperature (T) times entropy (S) value vs *degauss* values read from the self-consistent field calculation for Fermi–Dirac smearing, (d) variation of the temperature times entropy with temperature for single layers of WSeO (result is taken from a thermo_pw run with frozen ions option; namely, ions are not relaxed in each applied strain), WSeS, WSeSe, and WSeTe, (e) *ab initio* molecular dynamics results show a variation of the ion temperature with time for single layers of WSeO, WSeS, WSeSe, and WSeTe (NVT ensemble, Nosé–Hoover thermostat with a target temperature of 300 K, time step is one in the Hartree atomic units).

temperature scales with the finite temperature as it is defined in the WannierTools, this can justify the increasing inductive character of WSeO and WSeS single layers because we determine the *y*-axis values based on the *degauss* value to understand the characteristics of a meminductive system. As it is discussed above, we interpret Fig. 13(c) to compare the single layers; in terms of how big or small the variations in $-TS$ when we change the *degauss* will be important to determine how large the hysteresis is, namely, the area in between the curves constituting the hysteresis plot. However, this approach may not allow us to do exact quantitative comparisons between degauss and temperature.

E. Dynamics of phase-change like memory elements

After determining the *IV*-like curves of the single layers by using polarization vs *degauss* plots in Figs. 10(a), 10(b), and 10(d), we associate the IV-like characteristics of WSeS in Fig. 11(e) to a phase-transition like memristive mechanism's IV characteristics. In this way, we opt to use the ON and OFF notation used for phase-change memories, where this notation is given in Fig. 10(f). In analogy to a phase-change memory as described by Le Gallo and Sebastian, we believe that there are amorphous OFF state until the first threshold; after this, there is a bistable transition called amorphous ON following a memory switch and a crystalline ON state.[55] This on–off like switching suggests a phase-transition like memristive mechanism, but in our case, this is a phase-transition like mechanism without a change in the crystal symmetry. Since there is no real phase transition in our material, this ON–OFF cycle will continue, such as second, third, and so on, which might be regarded as oscillations. Therefore, we could not define exactly two distinct states, such as ON and OFF, over time in the absence of the applied bias. Therefore, we believe that the bacteria's so-called post-synapses resemble characteristics of artificial neurons of human rather than the synapses of the human because it is shown that the human neural characteristics can be emulated as a volatile memory element in the literature as well.[56,57] This leads us to argue about a phenomenon similar to *degauss* driven volatile resistive switching.

We study the response of these single layers to an impulse electric field using a time-dependent DFT tool as explained in Sec. II. We observe chaotic oscillatory behavior of the so-called ON and OFF states in the polarization vs time plot as shown in Fig. 13(a), even though the electric field is not oscillatory. As defined by Kumar *et al.*, these oscillations may indicate a higher-order of complexity. The possible chaotic behavior as a result of the coexistence of memcapacitor and meminductance is further investigated by matching these variables to the ones defined in an exemplary device in the literature. State variables of this exemplary device in the literature were temperature, charge on an internal capacitor, and speed of the Mott transition; we are required to define at least three state variables for our system.[57] We believe that these state variables might be charge, electronic temperature, and susceptibility based on the systems governing equation given by Eq. (5). In our model, we believe that the charge on the internal capacitor corresponds to an electric field, the electronic temperature scales with the physical temperature, and the speed of the Mott transition corresponds to susceptibility roughly. However, each of the state variables can be simulated in DFT using the *degauss* parameter, namely, charge as the Fermi level variations with respect to a reference level, temperature through electronic temperature with Fermi–Dirac occupations, and the Mott transition rate through the change of slope of IV-like curves when we tune the *degauss* parameter and through susceptibility of each single layer.

One of these state variables of a higher-order of a complexity system is given as the Mott transition rate in the exemplary system in the literature as discussed above. We claim that we may also define something linked with the Mott transition rate in our simulation protocol. In this way, we need to observe a change from a metal like to a non-metal like behavior through the variations in the conductivity with respect to temperature. In this way, we investigate the conductivity changes in WSeS from its polarization vs *degauss* and IV-like plot, where *degauss* represents the electronic temperature. When we consider line I in Fig. 11(e), WSeS acts as a semiconductor or insulator because conductance increases with temperature, where the conductance is taken as current over voltage and *degauss* is taken as proportional to the electronic temperature. In line II, it acts as a metal, where the conductance increases with decreasing temperature. Similarly, in line III, it acts as a metal, and in lines IV and V, it acts as a semiconductor or an insulator. We detect a change from a metallic character to a semiconducting or insulating character in between lines III and IV. This transition is observable in other single layers and differs from a single layer to a single layer. We also observe negative differential resistance like behavior in our simulation when we consider lines II and III in Fig. 11(e).

We suspect that simulation results show a phase-change like mechanism without a change in the crystal symmetry. This phase-change like mechanism might be analog to a measurement-induced phase transition, MIPT, as it is described in the literature.[59] This transition is governed by quantum many-body physics and quantified using quantum information dynamics. We try to connect this phenomenon to our system; therefore, we need to calculate a variable belonging to quantum information theory, that is, the entanglement entropy, but we can only calculate its classical analog, namely, entropy of the systems with DFT. Even though $-TS$ is not equal to entropy, we consider this value read from the self-consistent field calculations. We try to link the simulation results belonging to single layers to the definition of MIPT. By definition, in MIPT, entanglement growth shows different scaling laws with a change in the measurement rate.[59] If we consider one of the state variables of the higher-order of a complexity system as χ, which was previously thought as analog to the Mott transition rate as shown in a work with a memory device exhibiting higher-order of complexity in the literature, we may define χ in the framework of MIPT as the measurement rate by assuming the measurement rate as the slope of the polarization difference vs *degauss* plot, which can be written as $P/degauss$ and is equal to $\varepsilon_o\chi$ when we consider *degauss* as equal to an electric field.

MIPT is tried to be revealed from single layer's polarization vs *degauss* plot of each single layer. We can assume the variations in susceptibility based on the *degauss* parameter. Since *degauss* is correlated with the electronic temperature, we can consider decreasing susceptibility with *degauss*. Moreover, based on the $-TS$ vs *degauss* relation, we can conclude that *degauss* is positively correlated with

the smearing term, $-TS$, of the total DFT energy. If we plot the variation in $-TS$ with respect to time, here, time can be taken as *degauss* because we are beginning from 0 *degauss* to 0.04 Ry *degauss* value in time in our model, we can observe that the plots can be depicted by different equations, such as linear and parabolic. For small values of *degauss*, it is linear, and for large *degauss* values, it might be regarded as it is in a parabolic relation with $-TS$. This indicates entanglement toward a high *degauss* value according to MIPT, which is in line with our previous arguments with dephasing and coherency. We observe the growth of entanglement as it is characterized by $-TS$. We can consider geometrical parameters of single layers at each *degauss* value, and we try to relate them with their $-TS$. However, it is very hard to show that the converged value of $-TS$ in each *degauss* value exhibits different scaling laws, even though we consider the converged value of $-TS$ as the one found at the respective *degauss* value. There is one option to relate it to the geometry of the sample by considering additional charges or depletion of charges with varying *degauss* values through piezoelectricity. Making these single layers, a system resembling MIPT may let us discuss about the quantum many-body physics, but this is out of scope of this paper. However, we believe that this will be mainly linked to *d*-orbitals of transition metals in WSeO, WSeS, WSeSe, and WSeTe single layers.

F. Gene regulatory network and cellular memory and learning

In our model, bacteria's membrane is open to exposure from the outside environment. This will lead us to consider this system as an open system, where the entropy increases from WSeO to WSeSe and then decreases from WSeSe to WSeTe. Environmental perturbation to bacteria's membrane might be the strain. Its sensory receptor is located in its membrane, which is mainly responsible to generate a signal to trigger some enzymes and initiate the genetic transcriptions, where these gene transcriptions and protein synthesis are important to understand the memory in single-celled organisms.[8,60] The growth of bacteria is investigated in the field of evolutionary and developmental biology. This branch of biology is mostly explained by gene regulatory networks, which is also used to explain the adaptation of bacteria.[61–63] Dynamics of these gene regulatory networks are explained in the literature using a mathematical model as given in Eq. (13),

$$\frac{1}{\gamma_x}\frac{dx}{dt} = -x + \frac{k_m}{\gamma_x}\frac{k_x}{\gamma_m}c(x), \tag{13}$$

where it was assumed that mRNA degrades faster than the protein in the self-regulatory network, k_x is the mRNA to protein translation rate, γ_x is the degradation rate of protein, γ_m is the degradation rate of mRNA, b is the control parameter and is equal to k_x/γ_m, $c(x)$ is the input function, k_m is the transcription rate, x is the amount of protein, and m is the amount of mRNA.[58]

Gene regulatory network's model depicted in Eq. (13) looks like our model system's governing equation in Eq. (3). Therefore, we match the system's governing equation in Eq. (3) with the bacteria's gene regulatory network's governing equation in Eq. (13) by writing Eq. (3) as Eq. (14) given below:

$$(\chi/\dot{\chi})\dot{\mathscr{E}} = -\mathscr{E} + (\chi/\dot{\chi})(\dot{\bar{\varepsilon}}/\bar{\varepsilon})\mathscr{E}. \tag{14}$$

We matched the terms in Eq. (13) and in Eq. (14). We equate the terms as $1/\gamma_x$ is equal to $\chi/\dot{\chi}$, x is equal to $\mathscr{E}$, and $(k_m k_x/\gamma_m)c(x)$ is equal to $(\dot{\bar{\varepsilon}}/\bar{\varepsilon})\mathscr{E}$. The latter can be rewritten as in Eq. (15),

$$k_m b c(x) = (\dot{\bar{\varepsilon}}/\bar{\varepsilon})\mathscr{E}. \tag{15}$$

We can guess k_m as equal to $(\dot{\bar{\varepsilon}}/\bar{\varepsilon})$ because it is the only variable on the right-hand side with the $[T]^{-1}$ dimension, where T is time. On the other hand, x is equal to $\mathscr{E}$ and $c(x)$ is known to be the multivariable function of $\mathscr{E}$. The control parameter, b, is unitless, and we took it as χ because $\bar{\varepsilon}$ is already assigned to another variable. Hence, $c(x)$ is taken equal to $\mathscr{E}/\chi$ from Eq. (15). Hysteresis and non-stability of this system and, therefore, the memory effect can be seen from the x vs b plot, which is the $\mathscr{E}$ vs χ plot. Here, χ is defined as the feedback strength.[64] The reason why we consider χ the feedback strength is linked with its dependence to temperature. We attribute χ as it controls the response of the system to an external disturbance like the time-varying and oscillating electric field.

We expect to observe instability in the $\mathscr{E}$ vs χ plot. We can plot this graph from Fig. 11(e) by assuming direct proportionality between voltage and electric field and inverse proportionality between χ and temperature. If we consider each single layer in time in the outer cycle as shown in Fig. 3, we can also observe the oscillatory appearance in its x vs b relation. These oscillations are linked with the learning and memory abilities of biological systems, which also imply feedback loops, such as in a gene regulatory network.[44,65] We can consider the bacteria's gene regulatory system as something used to explain how bacteria are adapting itself under an environmental perturbation to survive.[66] We try to depict this system in a simple diagram, even though the bacteria's response and behavior are more complex than this description. We consider $c(x)$ as the input, x as the output, and b as the feedback strength. In Fig. 14, we depict this relation as a diagram. This diagram begins with the input, and this is assumed to trigger some proteins to initiate the transcription. After this, there will be a translation and the output protein is assumed to feedback the initiation of DNA to start the transcription process.

Modification of responses according to past abilities of living organisms are indications of learning, memory, and adaptation; as a result, in a single layered organism, previous experiences are important to modify its future behaviors.[60] In this way, we design a simulation protocol to understand how the model system, single layers, can mimic the behaviors of single-celled organisms. In this simulation, we try to replicate Bergstrom's experiment. Approximately 50 years ago, Bergstrom carried out experiments in a single-celled *Tetrahymena* in a laboratory environment to understand the learning and memory.[67] If we speak roughly, in that work, light flashes and electric shocks are used initially, and then animal is exposed to light only and its displacement is observed between these two cases. We adapt this experiment by changing electric shock with strain and light with solvent. We try to understand how much the susceptibility of a single layer will change between two cases.

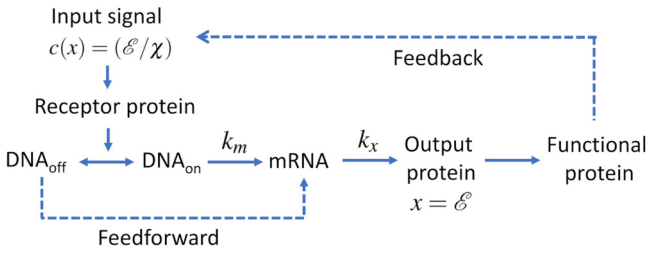

FIG. 14. Gene regulatory network's representative diagram drawn based on a diagram in the literature,[58] with feedback and feedforward mechanisms, depicted from an input signal to an output protein, where $c(x)$ is the input and x is the output protein.

We carry out a simulation to understand how the cellular memory and learning abilities of bacteria can be mimicked in single-layer WSeSe under strain. This simulation composed of case one and case two is shown in Fig. 15 from (a) to (d) with its corresponding Bergstrom's experiments. Case one represents the single layer under strain in the z-direction in a solvent environment as implemented in the Environ module, and case two represents the single layer without applied strain in a solvent environment as implemented in the Environ module. The applied strain or exposing single layers to a solvent will affect the properties of the membrane, therefore, the susceptibility response. We try to observe the difference between the susceptibility values in case one and case two. We calculate the difference between the susceptibility tensor's zz element read as 5%, 10%, and 15% strains and read as 0% strain, namely, the pristine one in different solvents. This difference is represented as $\Delta\chi_{zz}^{strain}$ (at a given μ) in Eq. (16),

$$\Delta\chi_{zz}^{strain}\big|_{at\ a\ given\ \mu} = \chi_{zz}(\bar{\varepsilon} = \bar{\varepsilon}_z, \mu) - \chi_{zz}(\bar{\varepsilon} = 0, \mu), \tag{16}$$

where χ_{zz} is the susceptibility matrix's diagonal element in the z-direction, μ is the optical permittivity, and $\bar{\varepsilon}$ is the strain. On the other hand, we calculate the difference between the susceptibility tensor's zz element read as solvent and read as vacuum in different strains. This difference is represented as $\Delta\chi_{zz}^{solvent}$ (at a given $\bar{\varepsilon}$) in Eq. (17),

$$\Delta\chi_{zz}^{solvent}\big|_{at\ a\ given\ \bar{\varepsilon}} = \chi_{zz}(\bar{\varepsilon}, \mu = \mu_{solvent}) - \chi_{zz}(\bar{\varepsilon}, \mu = 1). \tag{17}$$

The comparison of susceptibilities between different cases is important because if we have a higher difference between the cases, this may indicate better learning abilities, similar to the Bergstrom experiment. A higher displacement of bacteria in the absence of electric shock indicates better learning, which increases with an increase in the applied electrical shock.

These differences in susceptibilities are read for three different applied strains of 5%, 10%, and 15%. All the susceptibilities are found from the TDDFT calculation at zero frequency belonging to the zz component of the susceptibility tensor. The strain is applied by keeping the ratio of vertical distances between the upper and lower chalcogen atoms as constant with respect to W in the unit

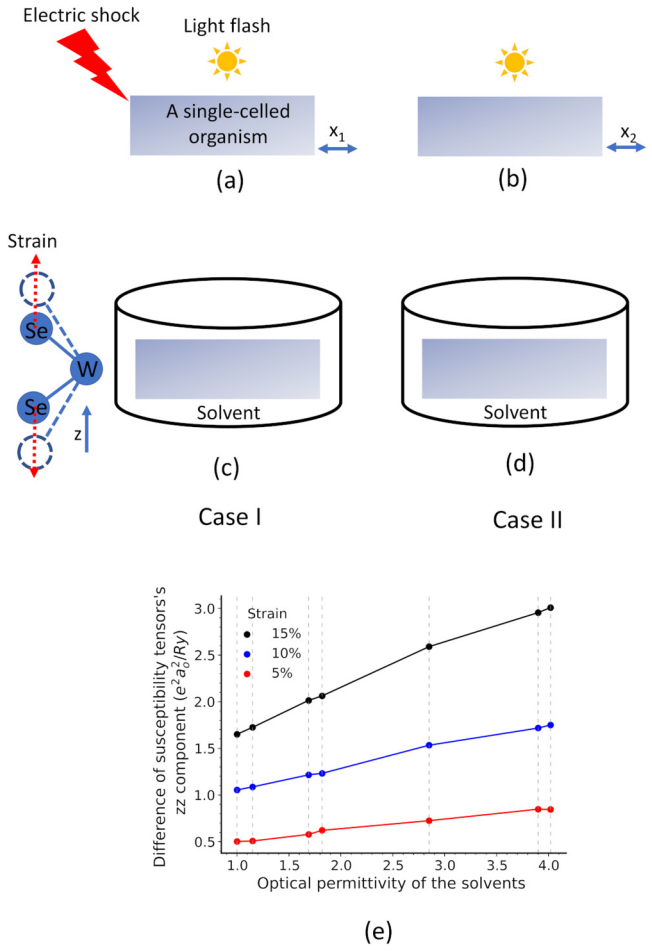

FIG. 15. Cartoons representing (a) case I of the Bergstrom experiment with electric shock and light flash applied to a single-celled organism, (b) case II of the Bergstrom experiment with light flash applied to a single-celled organism, (c) case I of the simulation done in this paper with strain and solvent applied to a WSeSe single layer, (d) case II of the simulation done in this paper with the solvent applied to a WSeSe single layer, and (e) the difference of the zz component of the susceptibility tensor of WSeSe read at zero frequency (with respect to zero percent applied strain) vs optical permittivity of the different solvents at 5%, 10%, and 15% strains.

cell. We conclude that the material remembers the susceptibility value it generates under strain and try to avoid the same susceptibility value even though we remove the strain. This is in line with Bergstrom's experiment because here, strain is something that can be understood as negative like shock in Bergstrom's experiment, where the electric shock is something to avoid for *Tetrahymena*. In this way, we plot $\Delta\chi_{zz}^{solvent}$ (at a given $\bar{\varepsilon}$) vs $\mu_{solvent}$ relation in Fig. 15(e) to study bacterial learning and memory with our simulation parameters of susceptibility, strain, and optical permittivity of solvent. In Fig. 15(e), we observe the highest difference in susceptibilities in solvent nitrobenzene, which has an optical permittivity of 4.02, than the other solvents at a given strain. On the other hand,

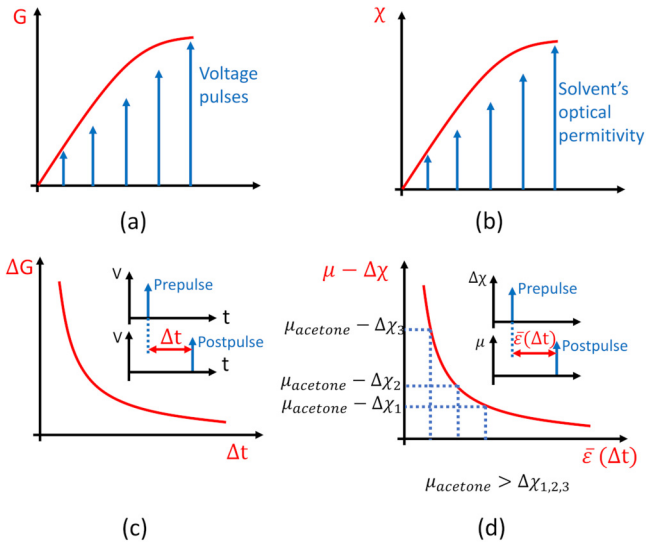

FIG. 16. (a) Potentiation plot, which is a characteristic of artificial synapses, depicts the conductance for different voltage pulses; (b) equivalent of an artificial synapse's potentiation plot, which depicts the susceptibility for different solvent's optical permittivity; (c) STDP's half plot, which is a characteristic of artificial synapses, depicts the conductance difference variation with time difference; and (d) equivalent of an artificial synapse's STDP plot, which depicts the solvent's optical permittivity–susceptibility difference with respect to strain.

in the highest strain, 15%, the susceptibility difference is higher than the 5% and 10% strained cases in Fig. 15(e) in all solvents since we consider the tensile strain as the growth of bacteria and the increase in the susceptibility difference indicates better learning abilities with time.

In the literature, artificial synapses are designed inspired from the human synapses; in these artificial synaptic materials, it is customary to show the potentiation of the synapses with discrete impulses. In Fig. 16(a), we depict a cartoon showing this potentiation, where discrete pulses are applied as an input and conductance is read as an output. We try to show this in our system as it is depicted in a cartoon in Fig. 16(b), where solvent's optical permittivity changes as discrete voltage pulses and the susceptibility is read as the conductance in Fig. 16(a). To replicate potentiation, we choose a WSeSe subsystem because it has continuum memory properties. We replicate the potentiation experiment by using different solvents, which has different optical permittivities. At a certain strain, susceptibilities are increasing and expected to reach a plateau like region with increasing optical permittivity of the solvent as shown in Fig. 17(a). We compare the potentiation of WSeSe in different strains by subtracting susceptibilities at optical permittivities of 4.02 from the susceptibilities read at an optical permittivity of 1. We saw the largest potentiation for the 15% strained case and the lowest in the 0% strained case. This result is in line with our previous discussion; specifically, tensile strain is the growth of bacteria and an increase in the susceptibility difference indicates better learning and memory abilities.

In artificial synapses, another commonly mimicked characteristic is the spike-time dependent plasticity, STDP, as depicted in a cartoon in Fig. 16(c), where the pulses are applied with a time difference to pre- and post-synaptic terminals and the change in conductance is recorded depending on the time difference. We replicate STDP by setting the time difference as the strain applied to the material in time and the conductance difference as the difference between the solvent's optical permittivity and the susceptibility difference with respect to 0%, $\Delta\chi_i$, where $i = 1, 2, 3$. In this way, we record the susceptibility differences for each solvent with respect to the vacuum susceptibility by varying the strain as shown in $\Delta\chi_{zz}^{strain}$ (at a given μ) vs strain plot in Fig. 17(b). The bigger the difference in susceptibility at a certain solvent is compared to vacuum, $\Delta\chi_i$, where $i = 1, 2, 3$ the bigger the strain is. Here, we assumed that the increased strain in the z-direction increases $\Delta\chi_i$, where $i = 1, 2, 3$. The difference between the solvent polarity (here, polarity of the solvent is considered polarization) and $\Delta\chi_i$ decreases as we increase the strain as shown in Fig. 16(d).

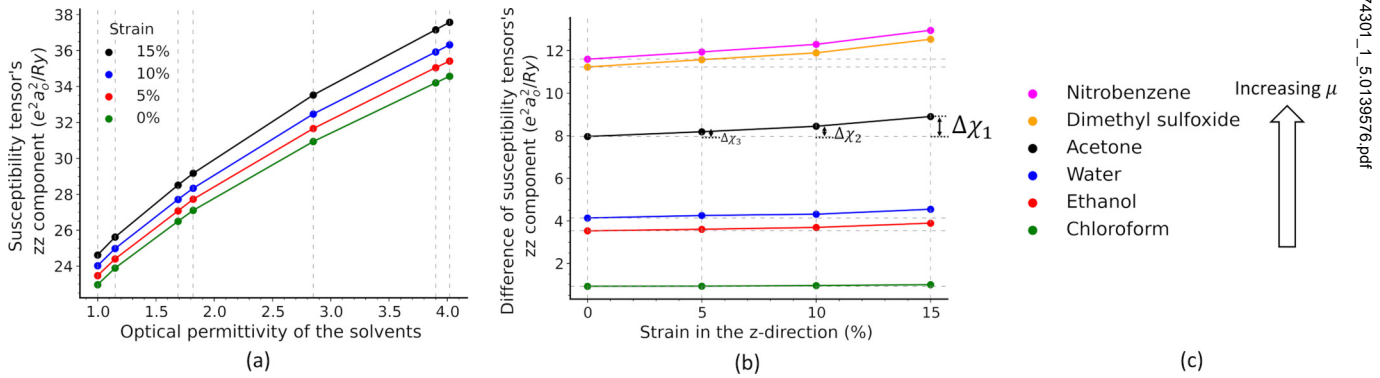

FIG. 17. (a) Susceptibility tensor's zz component at zero frequency vs optical permittivity of the different solvents drawn for different strains of WSeSe, (b) difference of the zz component of the WSeSe's susceptibility tensor at zero frequency (with respect to the vacuum) vs strain drawn for different solvents, and (c) solvent's optical permittivity increases from chloroform to nitrobenzene.

IV. CONCLUSION

We mimic the bacterial learning and memory abilities in a tungsten based two-sided single layers in time, which resembles a phase-change like pseudo-quantum memory element. We mimic these abilities as a function of growth in time by considering certain measurables, namely, observables, these are electric field, polarization, and strain, even though the real system dynamics are assumed to be governed by the quantum information theory. We consider the strain in the z-direction as the growth of the membrane, thereby the growth of bacteria, which can learn and develop learning and memory to survive by adaptation. This characteristic behavior of bacteria is observed to be very similar to bacteria in the literature, which is *Geobacter metallireducens*. We developed a simple model of the system, which can comply with the gene regulatory network's model above its governing equation. We reveal the cellular learning and memory abilities of the bacteria using TDDFT in different solvents.

We carry out DFT simulations in WSeO, WSeS, WSeSe, and WSeTe single layers, which indeed form a circuit. This circuit may show different memory element characteristics based on frequency, like in our case, different frequency represents a different single layer. This method of simulating materials at different times with different unit cells might be used to simulate flexoelectric materials, viscoelastic materials, and time crystals in the future. Mimicking bacterial learning and memory using 2D materials may allow us to study bacterial colonies using lateral heterostructures of two-dimensional materials, which might be beneficial to study antibiotic resistance in the future because this is linked with the learning and memory ability of the bacterial colonies against environmental stresses.

ACKNOWLEDGMENTS

Computing resources used in this work were provided by the National Center for High Performance Computing (UHeM) under Grant Nos. 1003272014 and 1012412022. The authors thank the Scientific Projects Unit (BAP) at Istanbul Technical University for the financial support of Aykut Turfanda's Ph.D. thesis (Project No. 43673) and the Turkish Higher Education Council (YOK) for 100/2000 Ph.D. stipend in the area of intelligent and innovative materials.

AUTHOR DECLARATIONS

Conflict of Interest

The authors have no conflicts to disclose.

Author Contributions

Aykut Turfanda: Conceptualization (equal); Investigation (lead); Methodology (equal); Visualization (lead); Writing – original draft (lead). **Hilmi Ünlü:** Conceptualization (equal); Investigation (supporting); Methodology (equal); Supervision (lead).

DATA AVAILABILITY

The data that support the findings of this study are available from the corresponding author upon reasonable request.

APPENDIX: HYDROGEN BOND MODEL, ELECTROSTATIC POTENTIAL ENERGY VARIATIONS, AND ORDINARY MAGNETORESISTANCE CALCULATIONS

We solve the one-dimensional Schrödinger equation numerically for the one electron problem with the potential describing the hydrogen bonding. This potential is the Duffing potential, $V(z)$, which is similar to a double-well potential, and it is given by Eq. (A1),

$$V(z)/V_r = \frac{1}{2}\alpha z^2 + \frac{1}{4}\beta z^4, \tag{A1}$$

where V_r is the potential, α and β are the variables, which are functions of d, and z is the coordinate in one dimension. A spatially discretized Schrödinger equation is obtained using a finite difference method, and it is given by Eq. (A2),

$$\frac{-\hbar^2}{2m}\frac{\psi_{i-1} - 2\psi_i + \psi_{i+1}}{(\Delta z)^2} + V_i\psi_i - E\psi_i = 0, \tag{A2}$$

where ψ is the wave function and Δz is the distance between the adjacent equidistant grid points, such as i and $i+1$. Converting Eq. (A2) into a matrix equation by defining $c = \hbar^2/2m(\Delta z)^2$ will allow us to write the principal diagonal elements of the discretized $N \times N$ Hamiltonian matrix as $2c + V_1, 2c + V_2, \ldots, 2c + V_N$, upper diagonal elements and lower diagonal elements as $-c$, and

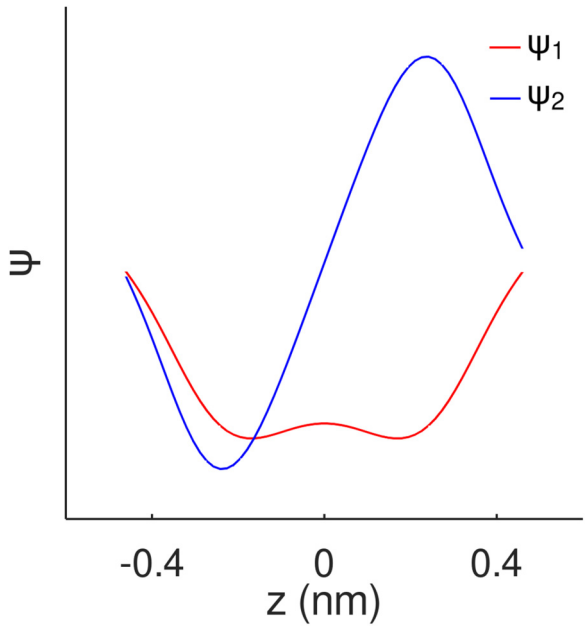

FIG. 18. Discretized wavefunctions for the two lower states, namely, ψ_1 and ψ_2, which is found from the solution of the eigenvalue problem.

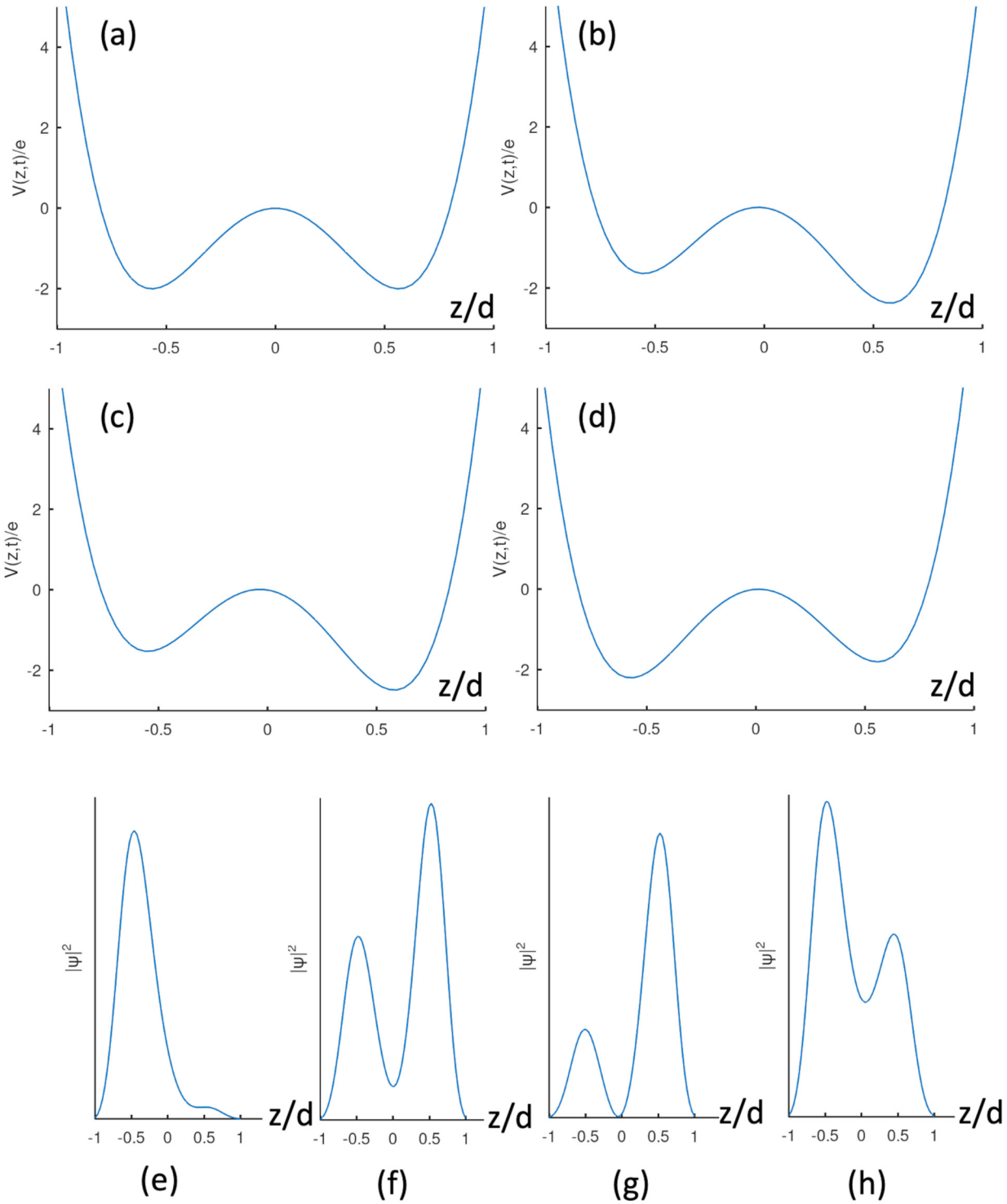

FIG. 19. Exemplary potential varies under a time-dependent electric field at time (a) $t(s)$, (b) $t + 0.5 \times 10^{-14}$ (s), (c) $t + 0.55 \times 10^{-14}$ (s), and (d) $t + 0.85 \times 10^{-14}$ (s); an exemplary solution of the time-dependent Schrödinger equation is given, which depicts the variations of the absolute value of the wave function square as a function of position at time (e) $t(s)$, (f) $t + 0.5 \times 10^{-14}$ (s), (g) $t + 0.55 \times 10^{-14}$ (s), and (h) $t + 0.85 \times 10^{-14}$ (s).

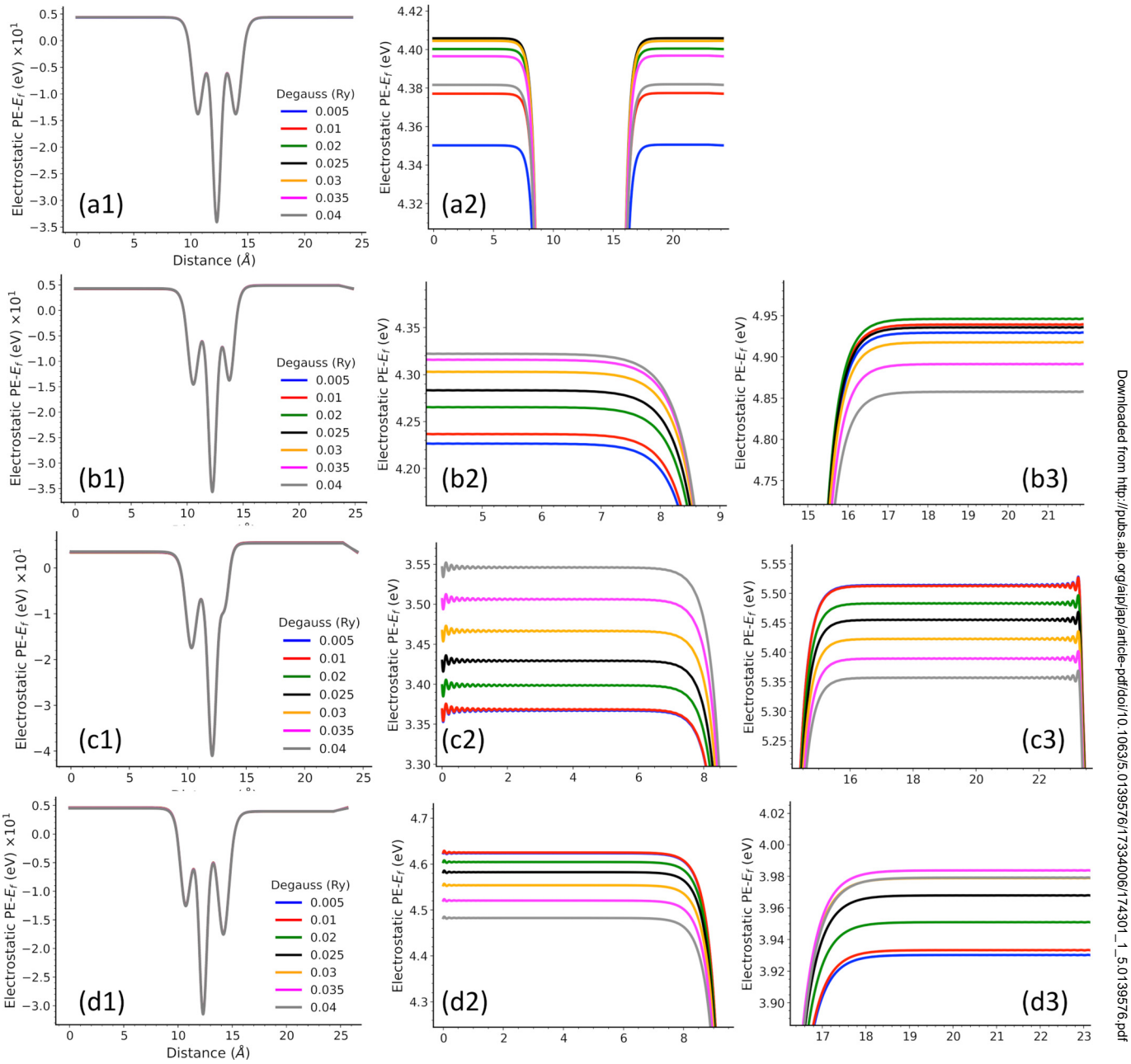

FIG. 20. Electrostatic potential energy E_f (eV) as a function of distance in the z-direction (Å) for tungsten based two-sided single layers of (a1) WSeSe, (b1) WSeS, (c1) WSeO, and (d1) WSeTe, where E_f is read from self-consistent field calculations. Enlarged plots are depicted in (a2) for WSeSe, (b2) and (b3) for WSeS, (c2) and (c3) WSeO, and (d2) and (d3) for WSeTe.

the rest as 0. The discretized wave function is a $N \times 1$ matrix with elements $\psi_1, \psi_2, \ldots, \psi_N$. We set the boundary vector to 0 for bound states by assuming boundaries at positive infinite and negative infinite in one dimension. Therefore, the solution of this eigenvalue problem gives the discretized wave functions. We plot the two lowest energetic states ψ_1 and ψ_2 as shown in Fig. 18.

To understand the interactions of these states, depicted by their wave functions, with a time-varying and oscillating electric

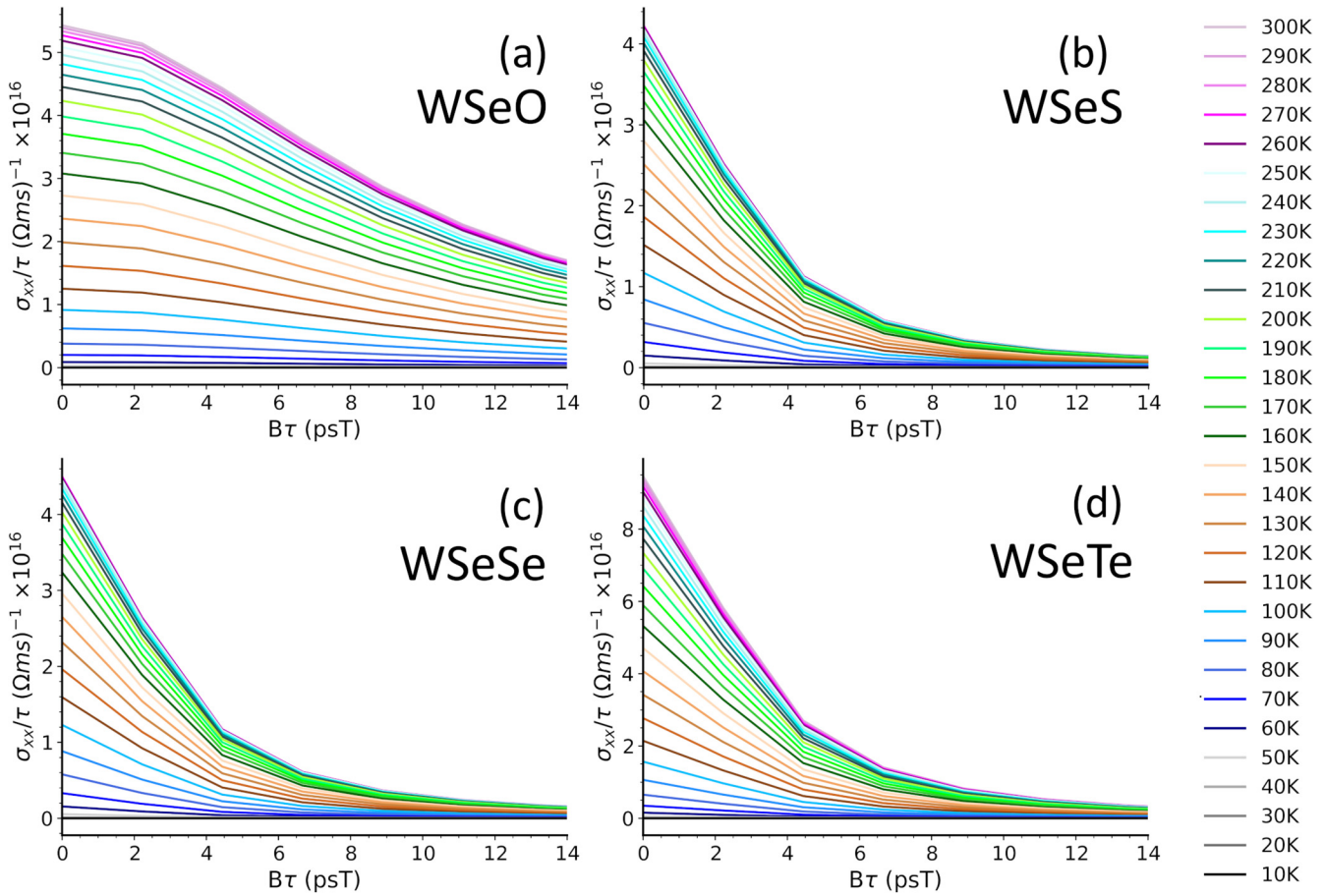

FIG. 21. Ordinary magnetoresistance calculations, σ_{xx}/τ, as a function of the magnitude of the magnetic field (B) in the z-direction for different temperatures for tungsten based two-faced single layers of (a) WSeO, (b) WSeS, (c) WSeSe, and (d) WSeTe, where we set the Fermi energy level 0.026 eV above the valence band maximum.

field, we consider time-dependent potential, $V(z, t)$, as given by Eq. (A3),

$$V(z, t) = V(z) - e\mathscr{E}z\sin(\omega t), \tag{A3}$$

where ω is the frequency and t is the time. To obtain the space-time discretized one-dimensional Schrödinger equation, first, we spatially discretize the time-dependent Schrödinger equation. In a matrix representation, we obtain the principal diagonal elements of the discretized $N \times N$ Hamiltonian matrix, $\tilde{H}^n$, as $2c + V_1^n$, $2c + V_2^n$, …, $2c + V_N^n$, upper diagonal elements and lower diagonal elements as $-c$, and the rest as 0. The discretized wave function is a $N \times 1$ matrix with elements ψ_1^n, ψ_2^n, …, ψ_N^n. After that, we implement the Crank–Nicholson time-propagation scheme, and we obtain the propagation of wave function in time, $\tilde{\psi}^{n+1}$, as given by Eq. (A4),

$$\tilde{\psi}^{n+1} = \left(\tilde{I} + i\frac{\Delta t}{2\hbar}\tilde{H}^{n+1}\right)^{-1}\left(\tilde{I} - i\frac{\Delta t}{2\hbar}\tilde{H}^{n}\right)\tilde{\psi}^{n}, \tag{A4}$$

where the initial condition is taken as $\psi(t = 0) = (\psi_1 + \psi_2)/2$, $\tilde{H}^n$ is the matrix at time $t - \Delta t$, $\tilde{H}^{n+1}$ is the matrix at time t, and the superscript -1 on the right hand side represents the matrix inversion. During this simulation study, we will consider the following simulation parameters: an equidistant grid is chosen from $-d$ to $+d$, where d is set to 4.6 Å, the number of grid points is taken as 60, we took $\alpha = -25/d^2$ and $\beta = 625/8d^4$ in Eq. (A1), and we took $E = 0.2 \times 10^{10}$ V/m and $\omega = 2\pi\ (1.25) \times 10^{14}\ s^{-1}$ in Eq. (A3). Moreover, we consider $V_r = 1$ eV, $m = 9.10 \times 10^{-31}$ kg, and $e = 1.6 \times 10^{-19}$ C. An exemplary solution of the time-dependent Schrödinger equation is shown in Fig. 19, which depicts the variations of the absolute value of the squared wave function as a function of position over time, along with its corresponding potentials under a time-dependent oscillatory electric field. The

absolute value of the squared wave function represents the charge density, which can be considered an indication of a time-dependent dipole moment as shown in Fig. 19.

REFERENCES

[1]M. Lanza, H.-S. P. Wong, E. Pop, D. Ielmini, D. Strukov, B. C. Regan, L. Larcher, M. A. Villena, J. J. Yang, L. Goux, and A. Belmonte, "Recommended methods to study resistive switching devices," Adv. Electron. Mater. **5**, 1800143 (2019).

[2]S. Srivastava, *Understanding Bacteria* (Springer Science & Business Media, 2003).

[3]M. B. Akolpoglu, Y. Alapan, N. O. Dogan, S. F. Baltaci, O. Yasa, G. Aybar Tural, and M. Sitti, "Magnetically steerable bacterial microrobots moving in 3D biological matrices for stimuli-responsive cargo delivery," Sci. Adv. **8**, eabo6163 (2022).

[4]M. H. Abedi, M. S. Yao, D. R. Mittelstein, A. Bar-Zion, M. B. Swift, A. Lee-Gosselin, P. Barturen-Larrea, M. T. Buss, and M. G. Shapiro, "Ultrasound-controllable engineered bacteria for cancer immunotherapy," Nat. Commun. **13**, 1585 (2022).

[5]A. Loureiro and G. J. da Silva, "CRISPR-Cas: Converting a bacterial defence mechanism into a state-of-the-art genetic manipulation tool," Antibiotics **8**, 18 (2019).

[6]H. Tian, W. Mi, X.-F. Wang, H. Zhao, Q.-Y. Xie, C. Li, Y.-X. Li, Y. Yang, and T.-L. Ren, "Graphene dynamic synapse with modulatable plasticity," Nano Lett. **15**, 8013–8019 (2015).

[7]T. J. Ryan and S. G. Grant, "The origin and evolution of synapses," Nat. Rev. Neurosci. **10**, 701–712 (2009).

[8]R. D. Emes and S. G. Grant, "Evolution of synapse complexity and diversity," Annu. Rev. Neurosci. **35**, 111–131 (2012).

[9]S. G. Grant, "Computing behaviour in complex synapses: Synapse proteome complexity and the evolution of behaviour and disease," Biochemist **32**, 6–9 (2010).

[10]P. Giannozzi, S. Baroni, N. Bonini, M. Calandra, R. Car, C. Cavazzoni, D. Ceresoli, G. L. Chiarotti, M. Cococcioni, I. Dabo, and A. Dal Corso, "QUANTUM ESPRESSO: A modular and open-source software project for quantum simulations of materials," J. Phys.: Condens. Matter **21**, 395502 (2009).

[11]P. Giannozzi, O. Andreussi, T. Brumme, O. Bunau, M. B. Nardelli, M. Calandra, R. Car, C. Cavazzoni, D. Ceresoli, M. Cococcioni, and N. Colonna, "Advanced capabilities for materials modelling with Quantum ESPRESSO," J. Phys.: Condens. Matter **29**, 465901 (2017).

[12]P. Giannozzi, O. Baseggio, P. Bonfà, D. Brunato, R. Car, I. Carnimeo, C. Cavazzoni, S. De Gironcoli, P. Delugas, F. Ferrari Ruffino, and A. Ferretti, "Quantum ESPRESSO toward the exascale," J. Chem. Phys. **152**, 154105 (2020).

[13]D. R. Hamann, "Erratum: Optimized norm-conserving Vanderbilt pseudopotentials [Phys. Rev. B **88**, 085117 (2013)]," Phys. Rev. B **95**, 239906 (2017).

[14]D. Hamann, "Optimized norm-conserving Vanderbilt pseudopotentials," Phys. Rev. B **88**, 085117 (2013).

[15]H. J. Monkhorst and J. D. Pack, "Special points for Brillouin-zone integrations," Phys. Rev. B **13**, 5188 (1976).

[16]A. Jain, S. P. Ong, G. Hautier, W. Chen, W. D. Richards, S. Dacek, S. Cholia, D. Gunter, D. Skinner, G. Ceder, and K. A. Persson, "The materials project: A materials genome approach to accelerating materials innovation," APL Mater. **1**, 011002 (2013).

[17]S. Grimme, J. Antony, S. Ehrlich, and H. Krieg, "A consistent and accurate *ab initio* parametrization of density functional dispersion correction (DFT-D) for the 94 elements H-Pu," J. Chem. Phys. **132**, 154104 (2010).

[18]J. Perdew, K. Burke, and M. Ernzerhof, "Perdew, Burke, and Ernzerhof reply," Phys. Rev. Lett. **80**, 891 (1998).

[19]W. Kohn and L. J. Sham, "Self-consistent equations including exchange and correlation effects," Phys. Rev. **140**, A1133 (1965).

[20]D. Sangalli, A. Ferretti, H. Miranda, C. Attaccalite, I. Marri, E. Cannuccia, P. Melo, M. Marsili, F. Paleari, A. Marrazzo, and G. Prandini, "Many-body perturbation theory calculations using the Yambo code," J. Phys.: Condens. Matter **31**, 325902 (2019).

[21]A. Marini, C. Hogan, M. Grüning, and D. Varsano, "yambo: An *ab initio* tool for excited state calculations," Comput. Phys. Commun. **180**, 1392–1403 (2009).

[22]S. Maintz, V. L. Deringer, A. L. Tchougréeff, and R. Dronskowski, "LOBSTER: A tool to extract chemical bonding from plane-wave based DFT," J. Comput. Chem. **37**, 1030–1035 (2016).

[23]V. L. Deringer, A. L. Tchougréeff, and R. Dronskowski, "Crystal orbital Hamilton population (COHP) analysis as projected from plane-wave basis sets," J. Phys. Chem. A **115**, 5461–5466 (2011).

[24]A. Dal Corso, "Pseudopotentials periodic table: From H to Pu," Comput. Mater. Sci. **95**, 337–350 (2014).

[25]W. Tang, E. Sanville, and G. Henkelman, "A grid-based Bader analysis algorithm without lattice bias," J. Phys.: Condens. Matter **21**, 084204 (2009).

[26]I. Timrov, O. Andreussi, A. Biancardi, N. Marzari, and S. Baroni, "Self-consistent continuum solvation for optical absorption of complex molecular systems in solution," J. Chem. Phys. **142**, 034111 (2015).

[27]O. Andreussi, I. Dabo, and N. Marzari, "Revised self-consistent continuum solvation in electronic-structure calculations," J. Chem. Phys. **136**, 064102 (2012).

[28]G. Pizzi, V. Vitale, R. Arita, S. Blügel, F. Freimuth, G. Géranton, M. Gibertini, D. Gresch, C. Johnson, T. Koretsune, and J. Ibañez-Azpiroz, "Wannier90 as a community code: New features and applications," J. Phys.: Condens. Matter **32**, 165902 (2020).

[29]Q. Wu, S. Zhang, H.-F. Song, M. Troyer, and A. A. Soluyanov, "Wanniertools: An open-source software package for novel topological materials," Comput. Phys. Commun. **224**, 405–416 (2018).

[30]See https://dalcorso.github.io/thermo_pw/ for thermo_pw.

[31]K. Momma and F. Izumi, "*VESTA 3* for three-dimensional visualization of crystal, volumetric and morphology data," J. Appl. Crystallogr. **44**, 1272–1276 (2011).

[32]A. H. Romero, D. C. Allan, B. Amadon, G. Antonius, T. Applencourt, L. Baguet, J. Bieder, F. Bottin, J. Bouchet, E. Bousquet, F. Bruneval, G. Brunin, D. Caliste, M. Côté, J. Denier, C. Dreyer, P. Ghosez, M. Giantomassi, Y. Gillet, O. Gingras, D. R. Hamann, G. Hautier, F. Jollet, G. Jomard, A. Martin, H. P. C. Miranda, F. Naccarato, G. Petretto, N. A. Pike, V. Planes, S. Prokhorenko, T. Rangel, F. Ricci, G.-M. Rignanese, M. Royo, M. Stengel, M. Torrent, M. J. van Setten, B. V. Troeye, M. J. Verstraete, J. Wiktor, J. W. Zwanziger, and X. Gonze, "ABINIT: Overview, and focus on selected capabilities," J. Chem. Phys. **152**, 124102 (2020).

[33]H. Roy, K. Dare, and M. Ibba, "Adaptation of the bacterial membrane to changing environments using aminoacylated phospholipids," Mol. Microbiol. **71**, 547–550 (2009).

[34]R. Bright, A. Hayles, J. Wood, D. Palms, T. Brown, D. Barker, and K. Vasilev, "Surfaces containing sharp nanostructures enhance antibiotic efficacy," Nano Lett. **22**, 6724–6731 (2022).

[35]G. Kaim and P. Dimroth, "ATP synthesis by F-type ATP synthase is obligatorily dependent on the transmembrane voltage," EMBO J. **18**, 4118–4127 (1999).

[36]H. Strahl and L. W. Hamoen, "Membrane potential is important for bacterial cell division," Proc. Natl. Acad. Sci. U.S.A. **107**, 12281–12286 (2010).

[37]P. Marszalek, D. Liu, and T. Y. Tsong, "Schwan equation and transmembrane potential induced by alternating electric field," Biophys. J. **58**, 1053–1058 (1990).

[38]E. B. Jacob, I. Becker, Y. Shapira, and H. Levine, "Bacterial linguistic communication and social intelligence," Trends Microbiol. **12**, 366–372 (2004).

[39]R. King-Smith and D. Vanderbilt, "Theory of polarization of crystalline solids," Phys. Rev. B **47**, 1651 (1993).

[40]L. Bengtsson, "Dipole correction for surface supercell calculations," Phys. Rev. B **59**, 12301 (1999).

[41]G. Gould and L. Moraga, "A method for fitting the Fuchs-Sondheimer theory to resistivity-thickness measurements for all film thicknesses," Thin Solid Films **10**, 327–330 (1972).
[42]B. Kramer and A. MacKinnon, "Localization: Theory and experiment," Rep. Prog. Phys. **56**, 1469 (1993).
[43]M. Spagnolo, J. Morris, S. Piacentini, M. Antesberger, F. Massa, A. Crespi, F. Ceccarelli, R. Osellame, and P. Walther, "Experimental photonic quantum memristor," Nat. Photonics **16**, 318–323 (2022).
[44]S. E. Childers, S. Ciufo, and D. R. Lovley, "*Geobacter metallireducens* accesses insoluble Fe (III) oxide by chemotaxis," Nature **416**, 767–769 (2002).
[45]S. de Gironcoli, "Lattice dynamics of metals from density-functional perturbation theory," Phys. Rev. B **51**, 6773 (1995).
[46]J. Zhang, P. W. Hess, A. Kyprianidis, P. Becker, A. Lee, J. Smith, G. Pagano, I.-D. Potirniche, A. C. Potter, A. Vishwanath, and N. Y. Yao, "Observation of a discrete time crystal," Nature **543**, 217–220 (2017).
[47]J. Audretsch, *Entangled Systems: New Directions in Quantum Physics* (John Wiley & Sons, 2008).
[48]M. J. Verstraete and Z. Zanolli , "Density functional perturbation theory," in *Lecture Notes of the 45th IFF Spring School "Computing Solids: Models, ab initio methods and supercomputing,"* edited by S. Blügel, N. Helbig, V. Meden, and D. Wortmann (Forschungszentrum Jülich, 2014), Vol. 74, Chap. C2, pp. 1–29.
[49]L. Qingjiang, A. Khiat, I. Salaoru, C. Papavassiliou, X. Hui, and T. Prodromakis, "Memory impedance in TiO_2 based metal-insulator-metal devices," Sci. Rep. **4**, 4522 (2014).
[50]S. P. Adhikari, M. P. Sah, H. Kim, and L. O. Chua, "Three fingerprints of memristor," IEEE Trans. Circuits Syst. I: Regul. Pap. **60**, 3008–3021 (2013).
[51]Q. Wang, A.-A. D. Jones III, J. A. Gralnick, L. Lin, and C. R. Buie, "Microfluidic dielectrophoresis illuminates the relationship between microbial cell envelope polarizability and electrochemical activity," Sci. Adv. **5**, eaat5664 (2019).
[52]J. Han, C. Song, S. Gao, Y. Wang, C. Chen, and F. Pan, "Realization of the meminductor," ACS Nano **8**, 10043–10047 (2014).
[53]H. T. Ouboter, T. Berben, S. Berger, M. S. Jetten, T. Sleutels, A. Ter Heijne, and C. U. Welte, "Methane-dependent extracellular electron transfer at the bioanode by the anaerobic archaeal methanotroph "*Candidatus* Methanoperedens," Front. Microbiol. **13**, 1065 (2022).
[54]X. Wang, J. Yu, C. Jin, H. H. C. Iu, and S. Yu, "Chaotic oscillator based on memcapacitor and meminductor," Nonlinear Dyn. **96**, 161–173 (2019).
[55]M. Le Gallo and A. Sebastian, "An overview of phase-change memory device physics," J. Phys. D: Appl. Phys. **53**, 213002 (2020).
[56]A. Ram and A. W. Lo, "Is smaller better? A proposal to use bacteria for neuroscientific modeling," Front. Comput. Neurosci. **12**, 7 (2018).
[57]S. Kumar, X. Wang, J. P. Strachan, Y. Yang, and W. D. Lu, "Dynamical memristors for higher-complexity neuromorphic computing," Nat. Rev. Mater. **7**, 575–591 (2022).
[58]M. Pájaro, I. Otero-Muras, C. Vázquez, and A. A. Alonso, "Transient hysteresis and inherent stochasticity in gene regulatory networks," Nat. Commun. **10**, 4581 (2019).
[59]B. Skinner, J. Ruhman, and A. Nahum, "Measurement-induced phase transitions in the dynamics of entanglement," Phys. Rev. X **9**, 031009 (2019).
[60]A. Boussard, A. Fessel, C. Oettmeier, L. Briard, H.-G. Döbereiner, and A. Dussutour, "Adaptive behaviour and learning in slime moulds: The role of oscillations," Philos. Trans. R. Soc. B **376**, 20190757 (2021).
[61]A. Filloux, *Bacterial Regulatory Networks* (Caister Academic Press, London, UK, 2012).
[62]J. M. Requena, *Stress Response in Microbiology* (Caister Academic Press, Wymondham, Norfolk, UK, 2012).
[63]R. Gross and D. Beier, *Two-Component Systems in Bacteria* (Caister Academic Press, 2012).
[64]D. Angeli, J. E. Ferrell, Jr., and E. D. Sontag, "Detection of multistability, bifurcations, and hysteresis in a large class of biological positive-feedback systems," Proc. Natl. Acad. Sci. U.S.A. **101**, 1822–1827 (2004).
[65]D. B. Headley and D. Paré, "Common oscillatory mechanisms across multiple memory systems," npj Sci. Learn. **2**, 1 (2017).
[66]D. L. Shis, M. R. Bennett, and O. A. Igoshin, "Dynamics of bacterial gene regulatory networks," Annu. Rev. Biophys. **47**, 447–467 (2018).
[67]S. R. Bergström, "Induced avoidance behaviour in the protozoa Tetrahymena," Scand. J. Psychol. **9**, 215–219 (1968).
[68]X. Gonze, B. Amadon, G. Antonius, F. Arnardi, L. Baguet, J.-M. Beuken, J. Bieder, F. Bottin, J. Bouchet, E. Bousquet, N. Brouwer, F. Bruneval, G. Brunin, T. Cavignac, J.-B. Charraud, W. Chen, M. Côté, S. Cottenier, J. Denier, G. Geneste, P. Ghosez, M. Giantomassi, Y. Gillet, O. Gingras, D. R. Hamann, G. Hautier, X. He, N. Helbig, N. Holzwarth, Y. Jia, F. Jollet, W. Lafargue-Dit-Hauret, K. Lejaeghere, M. A.L. Marques, A. Martin, C. Martins, H. P. C. Miranda, F. Naccarato, K. Persson, G. Petretto, V. Planes, Y. Pouillon, S. Prokhorenko, F. Ricci, G.-M. Rignanese, A. H. Romero, M. M. Schmitt, M. Torrent, M. J. van Setten, B. Van Troeye, M. J. Verstraete, G. Zérah, and J. W. Zwanziger, "The Abinit project: Impact, environment and recent developments," Comput. Phys. Commun. **248**, 107042 (2020).